Science Paper

Controls on the Termination of Cretaceous Oceanic Anoxic Event 2 in the Tarfaya Basin, Morocco

Chiara Krewer[1][a], Simon W. Poulton[1], Robert J. Newton[1], Christian März[2], Benjamin J. W. Mills[1], Thomas Wagner[3]

[1] School of Earth and Environment, University of Leeds, [2] Institute for Geosciences, University of Bonn, [3] The Lyell Centre, Heriot-Watt University

American Journal of Science

Oceanic Anoxic Event 2 (OAE2) has been the focus of considerable research, but biogeochemical dynamics during the recovery from the carbon cycle disturbance largely remain unknown. Here, we present a high-resolution reconstruction of water column redox and nutrient cycling across the final stages of OAE2, in order to assess controls on the termination of widespread ocean anoxia. We focus on calcareous black shales deposited on a subtropical shelf at Tarfaya, Morocco, representing a location prone to water column anoxia beyond the temporal extent of the OAE itself. Our multi-proxy approach combining iron-sulfur systematics with redox-sensitive trace metal (U and Mo) concentrations documents persistent anoxia, with cyclic fluctuations between weakly euxinic (or possibly ferruginous) conditions and more intense euxinia. During the end of the carbon isotope plateau phase, elemental weathering ratios indicate muted variability in chemical weathering intensity, although fluctuating redox conditions may have been driven by changes in continental weathering inputs of sulfate and reactive iron. By contrast, during the recovery phase, changes in chemical weathering intensity appear to have exerted a strong control on redox fluctuations. Overall, the recovery phase documents progressively less reducing conditions and less intense chemical weathering, which resulted in decreased P recycling and intervals of P drawdown, as indicated by P phase partitioning results. These trends were interrupted by the Holywell Event, during which more intense euxinia and enhanced P recycling transiently returned during an interval of particularly low chemical weathering. Nevertheless, the general trend towards lower P bioavailability in the water column, due to both sequestration of P in the sediments and a likely progressive decrease in P supply via continental weathering, appears to have exerted a major control on the recovery from oceanic anoxia in this shelf setting, and potentially on a global scale.

1. INTRODUCTION

During the Cretaceous, major perturbations to the global Earth system led to intervals of ocean deoxygenation (Arthur et al., 1987; Arthur & Sageman, 1994; Jenkyns, 1980; Schlanger & Jenkyns, 1976). One of the common features of these Oceanic Anoxic Events (OAEs) was enhanced burial of organic carbon (C_{org}). During OAE2 (Cenomanian-Turonian, ~94 Ma), widespread deposition of organic-rich marine sediment occurred, accompanied by a positive carbon isotope excursion (CIE; Scholle & Arthur, 1980). Enhanced organic carbon burial was an ultimate consequence of extreme greenhouse conditions during the Cenomanian-Turonian (Barron, 1983). High global temperatures were linked to large igneous province (LIP) emplacements (Leckie et al., 2002) and elevated volcanic degassing (Arthur

et al., 1985; Huber et al., 1995; Jones et al., 2021; Kuroda et al., 2007; Larson, 1991), and thus increased atmospheric CO_2 concentrations (Forster et al., 2007; O'Brien et al., 2017; Robinson et al., 2019; Sinninghe Damsté et al., 2010).

Long-term sea-level rise, starting in the early Cretaceous and reaching its high stand in the early Turonian (Haq, 2014; Schlanger & Jenkyns, 1976; Wilson et al., 2002), led to an expansion of epi-continental shelf areas, while an enhanced hydrological cycle (Huber et al., 2002) promoted an increased supply of weathered material and nutrients to coastal areas (Arthur & Sageman, 1994; Jenkyns, 2010; Pogge von Strandmann et al., 2013; Poulton et al., 2015), especially in low latitude locations (Beckmann et al., 2005). High primary productivity in surface waters led to enhanced burial of organic matter (OM) and the global positive CIE (Bowman & Bralower, 2005; Jarvis et al., 2011;

Scholle & Arthur, 1980; Tsikos et al., 2004; Voigt et al., 2006).

Ocean circulation patterns also changed during the mid-Cretaceous (Ladant et al., 2020; Poulsen et al., 2001; Robinson & Vance, 2012; Trabucho Alexandre et al., 2010), especially within the semi-restricted proto-North Atlantic. With the deepening of existing connections to the Tethys and Pacific Ocean, and the opening of the Equatorial Atlantic Gateway, a connection between the proto-North Atlantic and the South Atlantic was created (Donnadieu et al., 2016; Dummann et al., 2023; Friedrich & Erbacher, 2006; Poulsen et al., 2001; Ruvalcaba Baroni et al., 2014; Trabucho Alexandre et al., 2010). However, due to a lack of deep water connection and an assumed reduced turnover rate, water within the proto-North Atlantic basin was already low in oxygen compared to the Pacific Ocean (Monteiro et al., 2012). Conditioned by paleogeography, the increasing temperatures and enhanced nutrient input turned the proto-North Atlantic basin into a large-scale nutrient trap (Trabucho Alexandre et al., 2010). This promoted primary productivity in the surface waters of basins and coastal areas, leading to enhanced water column deoxygenation (Monteiro et al., 2012; Trabucho Alexandre et al., 2010).

Black shale deposition was particularly pronounced in the proto-North Atlantic during OAE2 at the Cenomanian/Turonian (C/T) boundary (~93.5 Ma; Jenkyns, 2010). The semi-restricted setting created optimal conditions for the deposition of organic rich sediments, as indicated by the coeval onset of a positive CIE and enhanced C_{org} burial (Jenkyns, 2010; Kuypers et al., 2002; Tsikos et al., 2004). However, some locations document the deposition of C_{org}-rich black shales before the onset of the global isotope excursion, pointing to the earlier regional development of dysoxic-anoxic conditions (Eldrett et al., 2014; Monteiro et al., 2012; Westermann et al., 2014). This was particularly the case in the Tarfaya basin, a marine shelf setting at the NW margin of Africa, which was a major site for C_{org} burial before, during and after OAE2 (Kolonic et al., 2005; Kuhnt et al., 1990). Here, independent organic and inorganic redox proxies (biomarkers, Fe-S systematics and redox-sensitive trace metal patterns) document expanded intervals of anoxic-sulfidic (euxinic) water column conditions, where euxinia periodically reached the base of the photic zone (Goldberg et al., 2016; Kolonic et al., 2005; Kuypers et al., 2002; Poulton et al., 2015; Sinninghe Damsté & Köster, 1998). However, a higher resolution study of the early stages of OAE2 at Tarfaya demonstrated that euxinia was periodically interrupted by the development of ferruginous (anoxic, Fe(II)-containing) conditions, linked to orbitally-driven changes in weathering inputs of reactive Fe and sulfate (Poulton et al., 2015).

The depositional model of Kolonic et al. (2005) suggests that enhanced trade winds controlled by eccentricity led to continental upwelling of nutrient-rich and oxygen-depleted water from deeper parts of the proto-North Atlantic, fuelling surface productivity. However, an additional driver for elevated productivity was extensive recycling of phosphorus (P) from the sediment into the water column, which occurred under both euxinic and ferruginous conditions

(Poulton et al., 2015). Indeed, the highest burial of P occurred just before the onset of OAE2, as documented in the Tarfaya Basin (Kraal et al., 2010; Mort et al., 2007), as well as in other shallow and deep locations in the proto-North Atlantic (Hetzel et al., 2009; van Helmond et al., 2014), Tethys and the Western Interior Seaway (WIS; Mort et al., 2007). This likely occurred due to the onset of enhanced weathering inputs, while P recycling from the sediments then decreased the burial of P in the overlying strata (Kraal et al., 2010; Mort et al., 2008; Poulton et al., 2015).

While the onset of OAE2 at Tarfaya has been well-studied, the termination and recovery have received little attention, and thus the drivers controlling the cessation of OAE2, both on a regional and global scale, remain debated. To address this, we present a high-resolution reconstruction of the recovery phase of OAE2 in the highly dynamic Tarfaya basin, which was a region particularly prone to the development of anoxia. With the use of a multi-proxy approach, we reconstruct local redox conditions and P recycling on short timescales, providing new insight into general controls on the termination of past, and potentially future, ocean deoxygenation events.

2. GEOLOGICAL SETTING AND SAMPLE MATERIAL

The Tarfaya basin is located on the NW African Atlantic margin (fig. 1A and B), where upper Cretaceous sediments reach a total thickness of ~700 m, and consist of dark-grey, laminated, organic-rich sediments alternating with carbonate-rich sections without lamination (Leine, 1986). In the mid-Cretaceous, the basin was a marine shelf setting open to the proto-North Atlantic, located at a latitude of ~15°N (Kolonic et al., 2005; Kuhnt et al., 2009; Lüning et al., 2004). The sedimentary succession records a complete and expanded OAE2 sequence with a total thickness of 17 m, and high accumulation rates during OAE2 allow paleoceanographic and geochemical investigation at centennial scale (Kuhnt et al., 2001). The sediment matrix is composed of micrite, faecal pellets and coccoliths, with occasional shell fragments and fish remains (Leine, 1986). Core samples were obtained from site S57 (fig. 1C), located near the shelf centre in the deepest part of the basin (~250–300 m paleo-water depth; Kuhnt et al., 2005; see Supplementary Information for more details of previous work on this location).

The sedimentary rocks from core S57 record the positive CIE characteristic of OAE2, showing an increase in the isotopic composition of C_{org} ($\delta^{13}C_{org}$) from −27.1 to −23.6‰ in phase A (onset and initial peak), followed by phase B (plateau), where $\delta^{13}C_{org}$ is maintained at −24.6 ± 0.4‰ (fig. 1D). Phase C captures the recovery from the CIE, with $\delta^{13}C_{org}$ dropping to about −27.8‰ (Kolonic et al., 2005; Tsikos et al., 2004). The sedimentary succession dominantly comprises calcareous mudstones with $CaCO_3$ generally >60 wt% (fig. 1D). Organic carbon contents range between 2–10 wt% before the onset of OAE2, then increase to ~16 wt% in phase A and up to 26 wt% in phase B (fig. 1D). Our focus is on the end of phase B and phase C, between
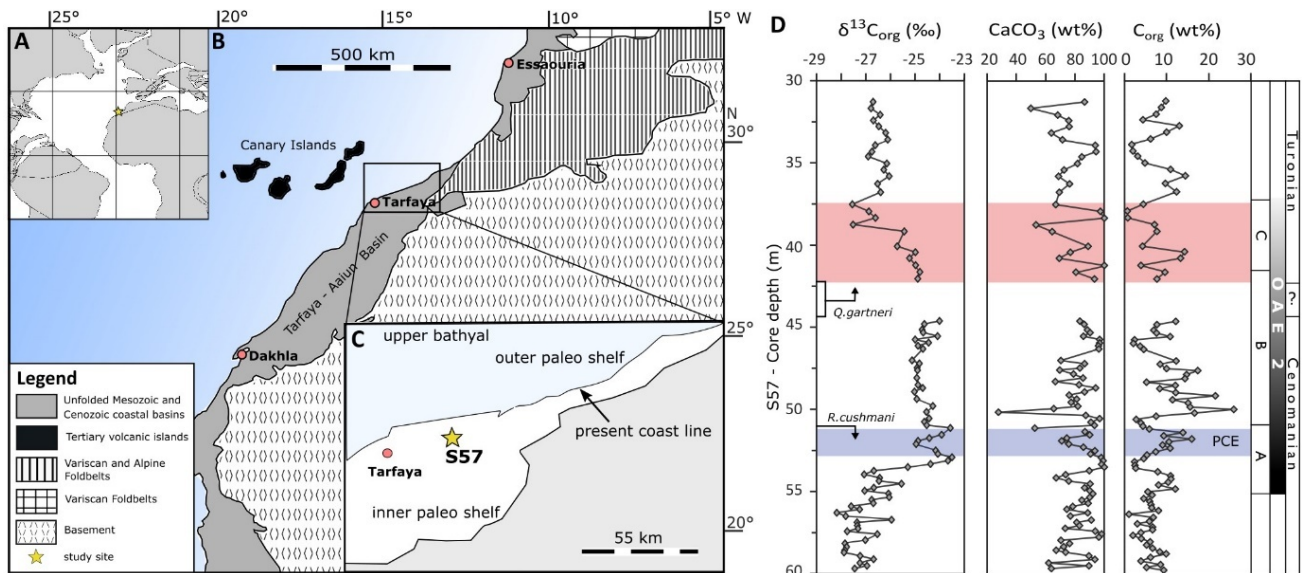
Figure 1. Location of the study site and bulk geochemical data through core S57. (A) Paleogeographic reconstruction of the proto-North Atlantic for the late Cretaceous (93.5 Ma, available at http://www.odsn.de/odsn/services/paleomap/paleomap.html) showing the location of the Tarfaya-Aaiun-Basin. (B) Detailed overview of the location of the Tarfaya-Aaiun-Basin and the surrounding geology, modified after Lüning et al. (2004). (C) Location of drill core S57, modified after Kolonic et al. (2005). (D) $\delta^{13}C_{org}$, $CaCO_3$ and C_{org} profiles for core S57. OAE2 phases A, B and C after Kuypers et al. (2002). $\delta^{13}C_{org}$ data from Tsikos et al. (2004), C_{org} and $CaCO_3$ data from Kolonic et al. (2005). Last occurrence of R. cushmani from Tsikos et al. (2004), and first occurrence of Q. gartneri from Kolonic et al. (2005). Pink bar highlights the section investigated in this study. Blue bar shows the Plenus Cold Event (PCE).

42.0 m and 37.5 m core depth, which has a maximum C_{org} content of ~15 wt%, while $CaCO_3$ ranges between 40 and 95 wt% (fig. 1D).

The investigated section shows no signs of turbidites, but some layers show shallow bioturbation at the centimetre scale (at 41.64–41.59 m, 40.94–40.91 m, 40.71–40.68 m and 37.57–37.55 m, fig. S2). The first occurrence (FO) of the nannofossilmarker *Quadrum gartneri* is used as a stratigraphic tool to locate the C/T boundary (Tsikos et al., 2004). However, for S57, missing sample material between 44.50 m and 42.04 m core depth likely coincides with the FO of *Quadrum gartneri*, placing the C/T boundary somewhere within this interval (fig. 1D). Based on sedimentation rates reported by Kuhnt et al. (1997), a duration of *ca.* 400 ka has been calculated for phases A and B of OAE2, while the duration of phase C was *ca.* 140 ka. The recovery in the $\delta^{13}C_{org}$ signal during phase C is characterized by a slow decline (fig. 1D).

3. METHODS

Core samples were taken at 1 cm resolution and every second sample was analyzed after crushing in an agate mill. Total sulfur (S_{total}), total carbon (C_{total}) and C_{org} were determined on a LECO C/S analyser. For C_{org}, samples were pre-treated with 10% (v/v) HCl to remove carbonate phases, and total inorganic carbon (TIC) was calculated as the difference between C_{total} and C_{org}. Replicate analyses of internal standards (LECO soil standard 502–982 with a carbon content of 22.7 ± 0.3 wt% and a S content of 0.321 ±

0.012 wt%; all errors are reported to 1σ) gave relative standard deviations (RSDs) of 1.5% for C_{org}, 1.1% for C_{total}, and 6% for S_{total}. Organic carbon isotopes were obtained using an Isoprime continuous flow mass spectrometer. The analyses were measured against a CO_2 reference gas and results are given in δ notation calibrated to the Vienna-Pee Dee Belemite (V-PDB) scale using UREA and sucrose laboratory standards of known and calibrated isotopic composition (UREA by Merck with $\delta^{13}C_{org}$= −46.83 ± 0.22‰; Silver Spoon sucrose (commercial) with $\delta^{13}C_{org}$= −26.19 ± 0.10‰; T&L sucrose (commercial) with $\delta^{13}C_{org}$= −11.93 ± 0.24‰). Standard reproducibility given by repeat analyses of the internal sucrose standard was better than 0.1‰. Sulfur isotopes were measured on Ag_2S precipitates ($\delta^{34}S_{py}$) from the chromous chloride extraction (see below) at 4 cm resolution. The results given in δ notation were calibrated to the international Vienna-Canyon Diablo Troilite (V-CDT) scale using a seawater laboratory standard (SWS-3) and a chalcopyrite inter-laboratory standard (CP1). These standards have known isotopic compositions of $\delta^{34}S$ = +20.3‰ and $\delta^{34}S$ = −4.56‰, respectively, which were calibrated using the international standard IAEA S-3, with an assigned $\delta^{34}S$ value of −32.06‰. Replicate analyses of all laboratory standards gave a precision of better than 0.2‰.

The total concentration of major and trace elements (Fe, Al, P, K, Na, Mo, U) were determined after an acid digestion (HNO_3-HF-$HClO_4$) of ground sediment samples ashed at 550°C. Major element concentrations were determined by ICP-OES, and trace elements were determined by ICP-MS, with RSDs of ≤2.9% and ≤4.3%, respectively. Accuracy was

determined relative to an international standard (Green River Shale, SGR-1), with 96 ± 5% for major elements and 93 ± 6% for trace elements.

Enrichment factors (EF) provide a useful way to consider trends in redox-driven trace metal draw down (for example, Algeo & Tribovillard, 2009; Tribovillard et al., 2006), and are commonly calculated as:

$$\text{Element}_{EF} = \frac{\text{Element}/\text{Al}}{\text{Element}_{UCC}/\text{Al}_{UCC}} \quad (1)$$

where UCC represents upper continental crust (for example, Wedepohl, 1995), although other compilations for average shale values can be used (Tribovillard et al., 2006). However, application of EF values to sediments rich in carbonate (and silica) is problematic, since the low detrital Al component typical for such (bio)chemical sediments leads to artificially elevated EF values relative to siliciclastic sediments (Tribovillard et al., 2006; Van der Weijden, 2002). One way around this problem is to consider excess element concentrations, which can be calculated as:

$$\text{Element}_{excess} = \text{Element}_{sample} - \left(\text{Al}_{sample} \times \frac{\text{Element}_{UCC}}{\text{Al}_{UCC}} \right) \quad (2)$$

However, while useful, excess trace metal values lack the utility of EF values as they provide no information on the relative degree of enrichment, and also cannot be directly compared to established techniques for identifying different paleoredox conditions (for example, Mo_{EF} vs U_{EF} crossplots; Tribovillard et al., 2012). To overcome these problems, we developed a new approach to calculate EF values for our carbonate-rich sediments by first calculating 'excess' trace metal values (eq 2), which we then use to calculate revised EF values (EF^*):

$$\text{Element}_{EF}^* = \frac{\text{Element}_{excess} + \text{Element}_{UCC}}{\text{Element}_{UCC}} \quad (3)$$

This approach overcomes the problem of low Al contents in chemical sedimentsand allows EF^* values to be directly compared to EF values calculated for siliciclastic sediments.

Iron speciation analyses were performed via standard techniques (Poulton, 2021; Poulton & Canfield, 2005) as detailed in table 1A. Steps I-III were performed sequentially, and Fe concentrations were determined by AAS. Steps IV and V were conducted on separate sample splits to determine sulfide-bound Fe (Canfield et al., 1986), where the mass of sulfide was determined stoichiometrically. The RSD for each extraction step is given in table 1, with accuracy (95 ± 2%) ensured relative to an international reference material (WHIT; Alcott et al., 2020). The total amount of Fe considered highly reactive towards sulfide (Fe_{HR}) is given by $\text{Fe}_{HR} = \text{Fe}_{carb} + \text{Fe}_{ox} + \text{Fe}_{mag} + \text{Fe}_{py}$, where Fe_{carb} represents Fe associated with carbonate minerals such as ankerite and siderite; Fe_{ox} represents Fe (oxyhydr)oxide minerals such as ferrihydrite, goethite and hematite; Fe_{mag} represents magnetite; and Fe_{py} represents pyrite (Poulton, 2021; Poulton & Canfield, 2005, 2011). Note that acid volatile sulfide (Fe_{AVS}) was below detection (<0.001 wt%) in all cases and is therefore not included in the Fe_{HR} calculation.

The SEDEX sequential extraction method (Ruttenberg, 1992; Thompson et al., 2019) quantifies four P-bearing phases in six sequential extraction steps (details given in table 1B), including: (1) P bound to easily reducible Fe (oxy-

hydr)oxides (P_{Fe1}), crystalline Fe (oxyhydr)oxides (P_{Fe2}) and magnetite (P_{mag}), with these phases combined to give P_{Fe}; (2) P associated with authigenic carbonate fluorapatite, biogenic apatite and P bound to $CaCO_3$ (P_{auth}); (3) P in detrital apatite (P_{det}); and (4) organic-bound P (P_{org}). The P concentration was determined spectrophotometrically via the phosphomolybdate blue method (Strickland & Parsons, 1972) for P_{auth} and P_{det}, or by ICP-OES for P_{Fe} and P_{org}. The total recovery of P, calculated as the sum of all extracted P phases relative to the bulk concentration (P_T), was 90.5 ± 5%, and RSDs are reported in table 1B (steps with higher RSDs reflect very low P concentrations in these pools). The P_{reac} pool, which is considered potentially mobile and bioavailable during deposition and early diagenesis, was calculated as $\text{P}_{reac} = \text{P}_{auth} + \text{P}_{Fe} + \text{P}_{org}$. Prior to the SEDEX method, a fish debris extraction (Schenau & De Lange, 2000) was applied on a set of samples to determine whether appreciable biogenic hydroxyapatite (P_{fish}) was present, which would complicate determination of P_{reac} concentrations. Samples were washed with 2 M NH_4Cl either 9 (n=30) or 12 (n=24) times. After each wash, P was determined spectrophotometrically.

We apply the Chemical Index of Alteration (CIA) proxy and K/Al ratios as indicators of the relative degree of chemical weathering on land. The CIA proxy is commonly calculated as $\text{CIA} = [Al_2O_3/(Al_2O_3 + Na_2O + K_2O + CaO^*)] \times 100$, where CaO^* reflects the concentration of CaO in silicates (i.e., corrected for Ca in carbonates and apatite; Fedo et al., 1995). However, given the very high carbonate content of the Tarfaya section, we took the common approach for such sediments of instead calculating CIA^*, where CaO^* is omitted (Flögel et al., 2008). During chemical weathering, labile elements (such as Na, K) are preferentially dissolved relative to immobile elements (e.g., Al), leading to elevated CIA ratios (Nesbitt & Young, 1982). By the same logic, lower K/Al ratios in marine sediments can also indicate higher intensity chemical weathering (for example, Garzanti et al., 2014; Harnois, 1988; Zabel et al., 2001).

4. INTERPRETATIONAL FRAMEWORK

4.1. Redox Reconstruction

In this study we utilise a variety of independent inorganic proxies to assess redox and nutrient cycling in the Tarfaya Basin. Using Fe speciation, the pool of Fe_{HR} is normalised to total Fe (Fe_T) to allow comparison between different settings (Poulton, 2021; Poulton & Canfield, 2005, 2011). While it is well-established that, wherever possible, redox-sensitive proxies should be independently calibrated to the particular study area (Algeo & Li, 2020; Poulton, 2021), extensive calibration of Fe speciation in a wide variety of modern and ancient settings has led to general thresholds that provide a first line of evidence to distinguish oxic and anoxic depositional conditions (Clarkson et al., 2014; Poulton, 2021; Poulton & Canfield, 2011; Poulton & Raiswell, 2002; Raiswell et al., 2001, 2018; Raiswell & Canfield, 1998). In this regard, oxic water column conditions are commonly indicated when $\text{Fe}_{HR}/\text{Fe}_T \leqslant 0.22$, in contrast to

Table 1. Fe (A) and P (B) sequential extraction steps.

Step	Reagents	Target Phase	RSD (%)
A Fe Speciation			
I	10 ml 1 M Na-acetate (pH 4.5, shake for 48 h at 50°C)	**Fe$_{carb}$**: iron associated with carbonates, incl. siderite and ankerite	3
II	10 ml Na-dithionite (50 g/L)/0.2 M Na-citrate (pH 4.8, shake for 2 h)	**Fe$_{ox}$**: reduced Fe(oxyhydr)oxides such as goethite and hematite	7
III	10 ml 2 M ammonium oxalate/0.17 M oxalic acid (shake for 6h)	**Fe$_{mag}$**: magnetite	6
IV	8 ml 50% HCl (boil for 1 h)	**Fe$_{AVS}$**: Fe bound as acid volatile sulfide	<LOD
V	15 ml 1 M chromous chloride dissolved in 50% HCl (boil for 1 h)	**Fe$_{py}$**: Pyrite	8
B P Phase partitioning			
I	10 ml Na citrate (882 g/L)/bicarbonate (84 g/L)/Na-dithionite (50 g/L) (shake for 8 h) 5 ml 1 M MgCl$_2$ (pH 8, shake for 2 h) 5 ml MilliQ water (shake for 2 h)	**P$_{Fe1}$**: P bound to Fe(oxyhydr)oxides and exchangeable P	6
II	10 ml 1 M sodium acetate (pH 4, shake for 6 h) 5 ml 1 M MgCl$_2$ (pH 8, shake for 2 h) 5 ml MilliQ water (shake for 2 h)	**P$_{auth}$**: carbonate-associated P, authigenic apatite and biogenic apatite	8
III	10 ml 1 M HCl (shake for 16 h)	**P$_{det}$**: detrital apatite and other inorganic P phase	10
IV	10 ml 2 M ammonium oxalate/0.17 M oxalic acid (shake for 6h) 5 mL 1M MgCl$_2$ (pH 8, shake for 2 h)	**P$_{mag}$**: P bound in magnetite	13
V	10 ml Na-dithionite (50 g/L)/0.2 M Na-citrate (pH 4.8, shake for 6 h) 5 mL 1 M MgCl$_2$ (pH 8, shake for 2 h)	**P$_{Fe2}$**: P bound to crystalline Fe oxides (hematite and goethite)	<LOD
VI	Ash at 550°C, 10 ml 1 M HCl (shake for 16 h)	**P$_{org}$**: organic P	8

ratios ≥0.38, which commonly occur due to additional water column precipitation of Fe$_{HR}$ phases under anoxic conditions (Raiswell & Canfield, 1998). Recognising that no strict threshold will satisfy all sedimentary environments, intermediate Fe$_{HR}$/Fe$_T$ ratios (between 0.22 and 0.38) are considered equivocal (Poulton & Canfield, 2011).

The ratio Fe$_{py}$/Fe$_{HR}$ can then be used to distinguish between euxinic and ferruginous settings (for anoxic samples), whereby ratios above 0.6–0.8 may indicate euxinia (T. F. Anderson & Raiswell, 2004; Benkovitz et al., 2020; März et al., 2008) and ratios ≤0.6 imply ferruginous conditions (Poulton, 2021; Poulton & Canfield, 2011). Here, we note recent challenges to the use of Fe speciation as a paleo-redox proxy (Pasquier et al., 2022). Indeed, particular care needs to be taken when Fe speciation is applied to sediments with low Fe contents (<0.5 wt% Fe$_T$; Clarkson et al., 2014), sediments experiencing rapid deposition (for example turbidites; Canfield et al., 1996), and those in proximity to hydrothermal inputs (Raiswell et al., 2018) or directly adjacent to (sub)tropical mountainous regions, where highly weathered sediment may supply a high proportion of Fe$_{HR}$ directly onto the continental margin (Wei et al., 2021), thus circumventing the preferential trapping of Fe$_{HR}$ that usually occurs in inner shore environments (Poulton & Raiswell, 2002). However, in addition to calibration in modern environments (Canfield et al., 1996; Raiswell & Canfield, 1998), Fe speciation has also been extensively calibrated in ancient settings (Clarkson et al., 2014; Poulton & Raiswell, 2002; Raiswell et al., 2001), which by definition have undergone the early diagenetic modification that Pasquier et al. (2022) claim compromises the proxy as a paleo-redox indicator. Furthermore, as also extensively discussed in the literature, Fe speciation is best used in combination with other indications of water column redox chemistry (for example, redox-sensitive trace metal systematics; Poulton, 2021).

We therefore consider our Fe speciation data alongside detailed analyses of redox-sensitive trace element (RSTE) concentrations (for example, Algeo, 2004; Algeo & Lyons, 2006; Algeo & Tribovillard, 2009; Hetzel et al., 2009; Tribovillard et al., 2006) to provide the most accurate assessment of the chemical conditions of deposition. In oxygenated modern oceans, the conservative elements Mo and U mainly occur as soluble molybdate (MoO$_4^{2-}$) and uranyl carbonate complexes (UO$_2$(CO$_3$)$_3^{4-}$; Tribovillard et al., 2006). Sediments deposited under oxic to dysoxic conditions commonly show no U enrichment, but under reducing conditions, U may be enriched following reduction to U(IV) (R. F. Anderson et al., 1989; McManus et al., 2005). Importantly, U enrichments do not require the availability of sulfide (Zheng et al., 2002), and hence occur under both ferruginous and euxinic conditions. However, molybdenum displays contrasting behaviour, whereby under anoxic conditions in the absence of sulfide, moderate Mo enrichments

may occur relative to U, via Mo drawdown through adsorption to Fe-Mn (oxyhydr)oxides in the water column (Algeo, 2004; Algeo & Lyons, 2006; Algeo & Tribovillard, 2009). In the presence of free sulfide, however, more extensive enrichments in Mo can occur via the formation and drawdown of thiomolybdate ($MoO_xS^{2-}_{4-x}$), which has a high affinity to sinking particles (Algeo & Lyons, 2006; Erickson & Helz, 2000; Helz et al., 1996; Tribovillard et al., 2004).

Thus, sedimentary enrichments in U and (possibly) Mo, coupled with elevated Fe_{HR}/Fe_T ratios (≥ 0.38), are highly indicative of deposition beneath an anoxic water column. Euxinia is indicated by a high accumulation of Mo, coupled with high Fe_{py}/Fe_{HR} ratios (in the range of 0.6–0.8 or above, for samples with $Fe_{HR}/Fe_T \geq 0.38$). Enrichments in U coupled with low Mo and low Fe_{py}/Fe_{HR} ratios (≤ 0.6, for samples with $Fe_{HR}/Fe_T \geq 0.38$), indicate either ferruginous conditions or possibly weak euxinia, with moderately elevated Mo concentrations indicating moderate euxinia.

4.2. Phosphorus Cycling

The bioavailability of P, the ultimate limiting nutrient for primary productivity on geological timescales (Tyrrell, 1999), exerts a strong control on ocean productivity and is hence closely linked to C_{org} burial and ultimately oxygen production (Guilbaud et al., 2020; Poulton, 2017; Van Cappellen & Ingall, 1994). Dissolved P delivered to the ocean by weathering is largely deposited in association with C_{org} and Fe (oxyhydr)oxides (Ruttenberg, 2003). However, the biogeochemical behaviour of P is strongly dependent on the redox state of the water column and sediments (Bowyer et al., 2020; Ingall & Jahnke, 1994; März et al., 2008; Van Cappellen & Ingall, 1994). Under oxic conditions in the water column, up to 90% of OM is commonly decomposed, releasing P back to the water column (Ingall & Jahnke, 1997; Ruttenberg, 2014). Under anoxic conditions, organic P (P_{org}) may be preferentially released from OM relative to C during microbial remineralization (Ingall et al., 1993; Ingall & Jahnke, 1994). Additionally, P associated with Fe (oxyhydr)oxides is released during reductive dissolution, either via dissimilatory Fe reduction (Thamdrup, 2000) or via direct reaction with dissolved sulfide (Canfield, 1989; Poulton et al., 2004). The preferential release of P from OM leads to elevated C_{org}/P_{org} ratios (Algeo & Ingall, 2007; L. D. Anderson et al., 2001), relative to the average Redfield Ratio of 106:1 (L. A. Anderson & Sarmiento, 1994; Redfield, 1958).

Bioavailable P that is released into porewaters under both oxic and anoxic conditions may be partially transformed into authigenic P phases such as carbonate fluorapatite (Ruttenberg & Berner, 1993) or vivianite (Xiong et al., 2019), which is known as '*sink switching*' (Slomp & Van Cappellen, 2007). Further, re-adsorption of recycled P on Fe (oxyhydr)oxides close to the redox boundary may lead to the additional retention of P in the sediment (Dellwig et al., 2010; Slomp et al., 1996). However, if free sulfide is present, either in the water column or in porewaters below an anoxic non-sulfidic water column, there is the potential for the dissolved P released via OM degradation and sulfide-

promoted Fe (oxyhydr)oxide reduction to diffuse back into the water column (Van Cappellen & Ingall, 1994).

To provide detailed insight into the potential significance of P recycling versus fixation in the sediment, we determined P_{org} and P_{reac} concentrations. The ratio C_{org}/P_{org} can be used to determine the extent of preferential P release during anoxic OM degradation (which gives high C_{org}/P_{org} ratios relative to the Redfield Ratio). By contrast, C_{org}/P_{reac} ratios indicate the extent of P retention versus recycling, whereby values close to the Redfield Ratio indicate a low recycling efficiency, and elevated values indicate P recycling. In addition, C_{org}/P_{reac} ratios below the Redfield Ratio indicate either additional P drawdown from the water column under anoxic conditions (for example, via adsorption to Fe (oxyhydr)oxides; Alcott et al., 2022; Guilbaud et al., 2020) or extensive OM oxidation and retention of the released P by microbial biomass under oxic conditions (Ingall & Van Cappellen, 1990).

5. RESULTS

5.1. Carbon Isotopes and Major Elements

The end of phase B is defined by a gradual return in $\delta^{13}C_{org}$ to pre-excursion values after the main phase of globally-enhanced C_{org} burial rates (Kuypers et al., 2002). Kolonic et al. (2005) placed the beginning of phase C at ~42.00 m depth (fig. 1D). However, our higher-resolution $\delta^{13}C_{org}$ profile is relatively stable until 40.15 m depth, with an average of -25.6 ± 0.16‰ (fig. 2). The $\delta^{13}C_{org}$ values then progressively decrease from -26.7‰ at 40.10 m to -27.9‰ at 37.49 m, thus placing the beginning of the recovery phase at 40.1 m (fig. 2). The decreasing trend is interrupted by a minor shift to more positive $\delta^{13}C_{org}$ values (up to -26.9‰) at 38.15-38.05 m depth, and a larger, well-defined positive shift (up to -24.9‰) between 37.79–37.69 m (fig. 2).

Darker layers in core S57 have elevated C_{org} (5–20.5 wt%) and lower $CaCO_3$ (50–75 wt%) contents, whereas lighter colored sections have higher $CaCO_3$ (up to 98 wt%) and lower C_{org} (<5 wt%) contents (fig. 2). In general, C_{org} and carbonate contents are inversely correlated, suggesting that the observed trends are controlled by the relative rates of production of each phase. Aluminium concentrations vary between 0.1 and 2.3 wt% (average 0.84 ± 0.5 wt%), with lower values at the end of phase B and higher values with more variation during the recovery phase (fig. 2). Concentrations of S_{total} vary between 0.1 and 3.5 wt% and follow the C_{org} trend. Organic S (S_{org}), calculated as the difference between S_{total} and pyrite S (assuming a negligible contribution from carbonate-associated S), shows that the majority of the total S is organically-bound (fig. 2). Concentration of K and Na are both low with a range of 0.03 to 0.84 wt% for K and 0.03 to 0.38 wt% for Na. While K shows a similar trend to Al, the concentration of Na is relatively stable throughout most of the section, with higher values in the uppermost 10 cm of the core (see fig. S2). Values for CIA* range between 50 and 85, while K/Al ratios are relatively stable (0.33 ± 0.02), with a minor gradual decrease up-section (from ~0.38 to ~0.32, fig. 2).
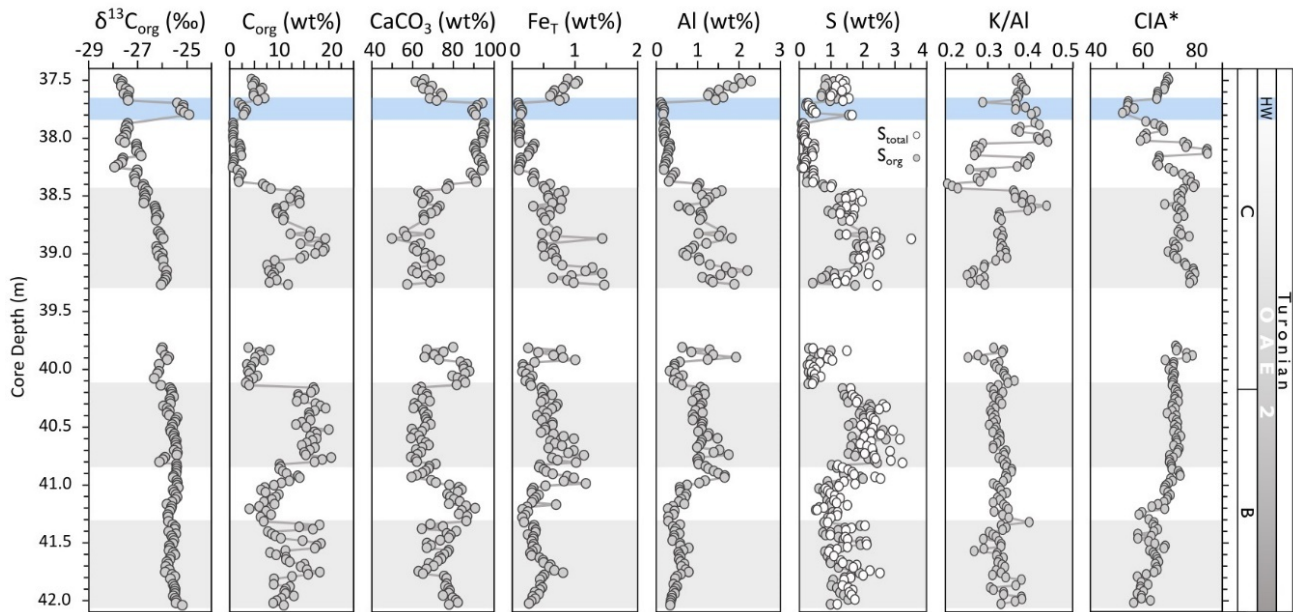
Figure 2. Bulk geochemical data and CIA* values for core S57. Sulfur is reported as total sulfur and organic sulfur (see text). Phases B and C are based on the $\delta^{13}C_{org}$ profile, representing the isotope plateau and recovery phase, respectively (Kolonic et al., 2005; Kuypers et al., 2002). The end of phase B is located further up-section than reported by Kolonic et al. (2005) as explained in the text. Grey shaded areas highlight intervals of high C_{org} concentration. The Holywell Event (HW) is highlighted in blue.

5.2. Redox Proxies

Iron concentrations range from 0.1 to 1.5 wt% with only minor fluctuations (average 0.51 ± 0.28 wt%), with 54% of the samples falling below 0.5 wt% (fig. 2). Since the concentration of Fe_T is relatively low, care has to be taken when evaluating Fe_{HR}/Fe_T ratios (Clarkson et al., 2014). However, unlike most of the carbonate units analyzed by Clarkson et al. (2014), which consisted of relatively pure limestones and dolomites, the Tarfaya samples dominantly comprise calcareous organic-rich sediments, with both OM and $CaCO_3$ constituting major diluting controls on elements such as Fe. Indeed, when calculated on a CH_2O-free basis, Fe_T concentrations average 0.72 ± 0.46 wt%, with 62% of the samples having >0.5 wt% Fe_T. Furthermore, Fe_{HR}/Fe_T ratios are persistently elevated throughout the section, regardless of Fe_T concentration patterns. In addition, as discussed below, the interpretation of redox conditions based on Fe_{HR}/Fe_T ratios is entirely consistent with that based on U_{EF}^* values (as an independent indicator of water column anoxia), while the interpretation of Fe_{py}/Fe_{HR} ratios is entirely consistent with that based on Mo_{EF}^* values (as an independent indicator of water column euxinia). Thus, as argued by Poulton et al. (2015) for phase A of OAE2 at Tarfaya, the Fe speciation data for these calcareous organic-rich sediments can be considered to provide reliable redox information.

The ratio of Fe_{HR}/Fe_T ranges from 0.4 to 0.9 (n=185) with only one sample falling within the equivocal zone (fig. 3, detailed concentration for each Fe pool in fig. S7). The ratio of Fe_{py}/Fe_{HR} varies between 0.4 and 0.8 (fig. 3). However, most samples (77%) fall within the 0.6–0.8 range. There is

no correlation between the Fe extraction results and C_{org} contents (fig. 3).

EF^*s for U and Mo are variable (fig. 3) but are persistently high throughout the section. The lower part of the section, between 42.04 m and 39.90 m, shows broad systematic changes in U and Mo concentrations, but in the upper part of the section (39.40 to 37.48 m), alternations between higher and lower concentrations occur across shorter intervals. In general, Mo concentrations show a strong correlation with C_{org} and S_{org} records, but a weaker relationship with pyrite-S concentrations (fig. 4). Enrichment factors are persistently elevated for both U (averaging 3.0 ± 1.0) and Mo (16.3 ± 11.3) (fig. 3). In general, the lower part of the section is characterized by the highest Mo_{EF}^* enrichments, and the amplitude of the peaks progressively decreases in the upper part of the section (fig. 3). Enrichments in U show trends that are similar to Mo in the lower part of the section, but U_{EF}^* values do not show the same overall decrease in the upper part of the section (fig. 3).

The $\delta^{34}S_{py}$ compositions show a wide range of values, between −27.3 and −4.0‰, but distinct trends in the data are apparent (fig. 3). The lower part of the section shows an overall increase from −27.3 to −8.7‰, with relatively little fluctuation, whereas the upper part of the section is characterised by larger, cyclical fluctuations (fig. 3).

5.3. Phosphorus

The total phosphorus concentration (P_T) ranges between 184 and 1494 ppm, with the highest values occurring in C_{org}-rich intervals (fig. 5). These data give average P_T/Al ratios of 0.1 ± 0.05 (in ppm/ppm), which is an order of mag-
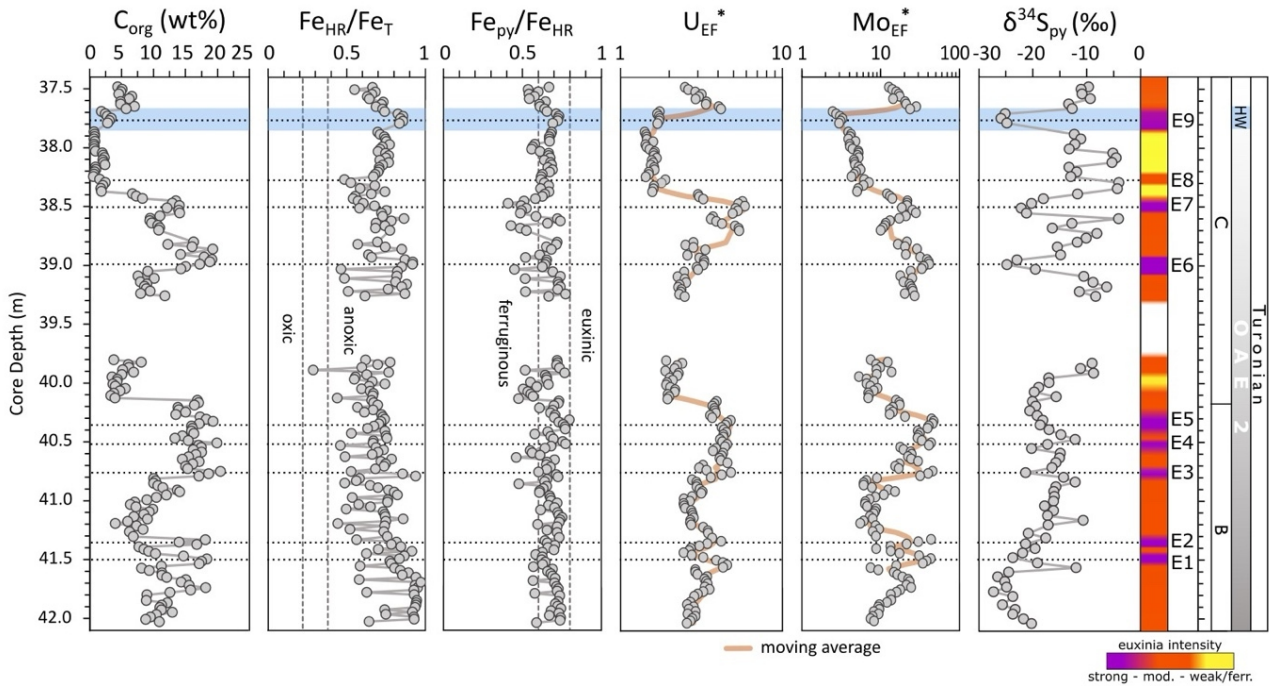
Figure 3. Redox proxy profiles, comprising C_{org}, Fe_{HR}/Fe_T and Fe_{py}/Fe_{HR} ratios, and enrichment factors (EF^*) for U and Mo. Orange solid lines represent the 5-point moving average. Vertical grey dashed lines indicate thresholds for oxic (0.22) and anoxic (0.38) depositional conditions (Fe_{HR}/Fe_T plot), and between ferruginous (0.6) and euxinic (0.8) depositional conditions (Fe_{py}/Fe_{HR} plot). Colored bar indicates intensity of water column redox conditions from strong/moderate (mod.) euxinia to weak/ferruginous (ferr.) as defined in the main text. Horizontal black dashed lines indicate peaks in episodes of strong to moderate euxinia.
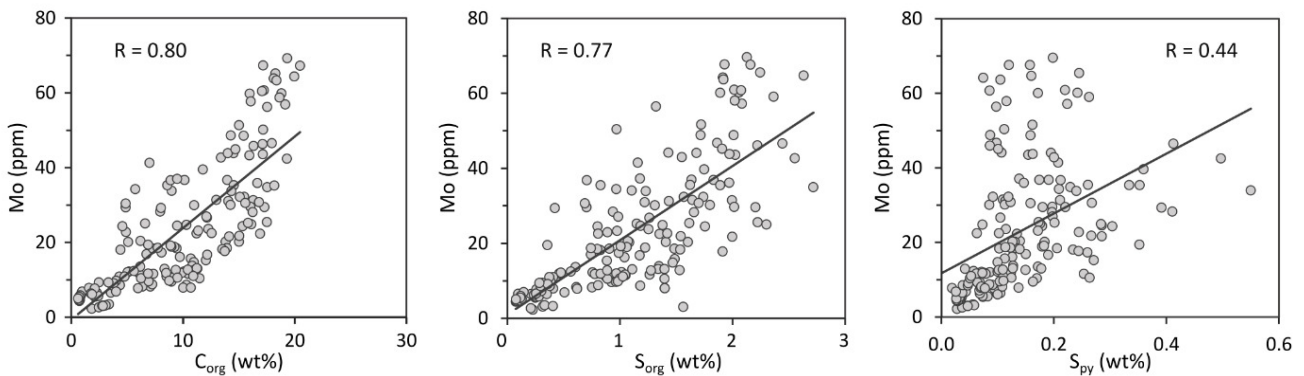

Figure 4. Plots of Mo versus C_{org}, Mo versus S_{org}, and Mo versus pyrite-S.

nitude higher than the UCC value of 0.01 (Wedepohl, 1995). In more detail, however, P_T/Al ratios are generally relatively constant in the lower part of the section, while the upper part of the section is characterized by more frequent pulsed intervals of elevated P_T/Al that are superimposed on an overall increasing trend, which is followed by a decrease at the very top of the section (fig. 5).

Data for the overall phase partitioning of P are displayed in figure 6. Concentrations of P_{Fe}, P_{det} and P_{org} are low and generally relatively constant (fig. 6). The largest P pool is P_{auth}, with concentrations of up to 1250 ppm, representing an average contribution of 87 ± 6% to P_T and 98 ± 1% to the P_{reac} pool. The quantification of P_{auth} has the potential to be slightly overestimated as the extraction step may

also include biogenic hydroxyapatite (fish debris) (Schenau & De Lange, 2000). We note, however, that P_{fish} comprises only 2.6 ± 3.2% of P_T in the analyzed samples, suggesting a minimal contribution from fish debris (fig. 6), which is consistent with the results reported by Kraal et al. (2010). Molar C_{org}/P_{org} ratios are above the Redfield Ratio throughout the section, with exceptionally high values in the lower part of the section (fig. 5). This is followed by a general decreasing trend towards the top of the core, with values that approach those more commonly found in ancient euxinic marine settings (for example, Alcott et al., 2022; Dijkstra et al., 2018; Mort et al., 2010; Reinhard et al., 2017; Slomp et al., 2004), although very high C_{org}/P_{org} ratios return during the small
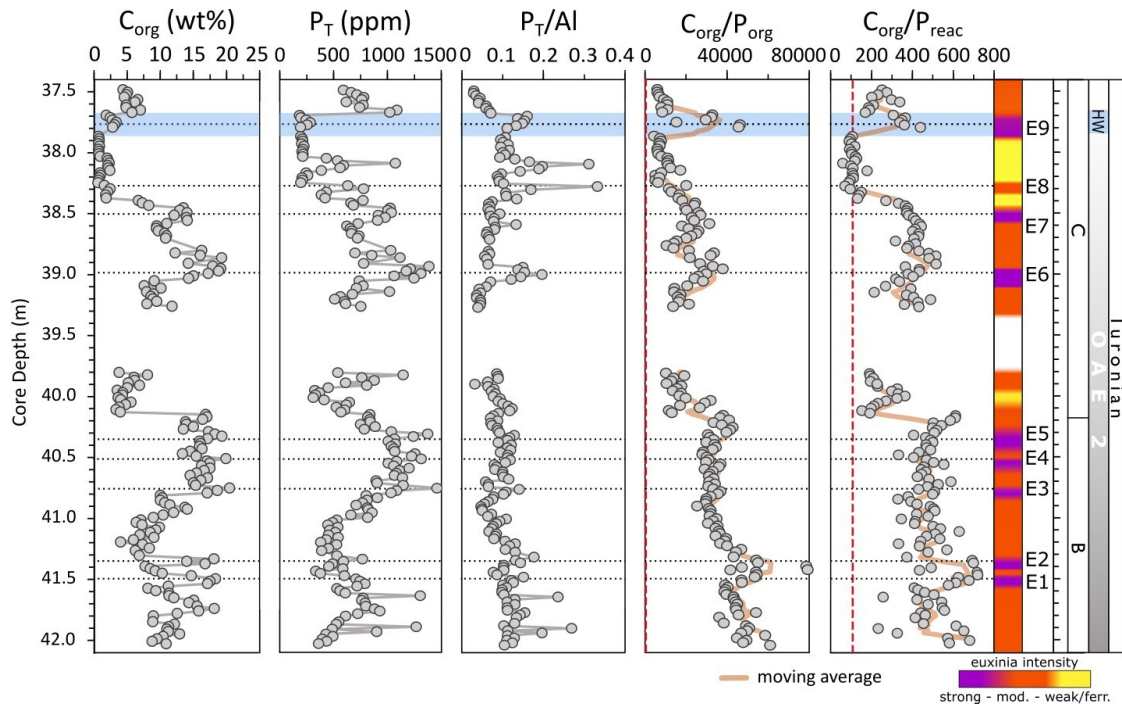
Figure 5. Total phosphorus (P_T) and C_{org} profiles through core S57, including P_T/Al ratios, and molar C_{org}/P_{org} and C_{org}/P_{reac} ratios. Orange lines are the 5-point moving average. Red dashed lines represent the Redfield Ratio (106:1). Colored bar for redox conditions as in fig. 3.
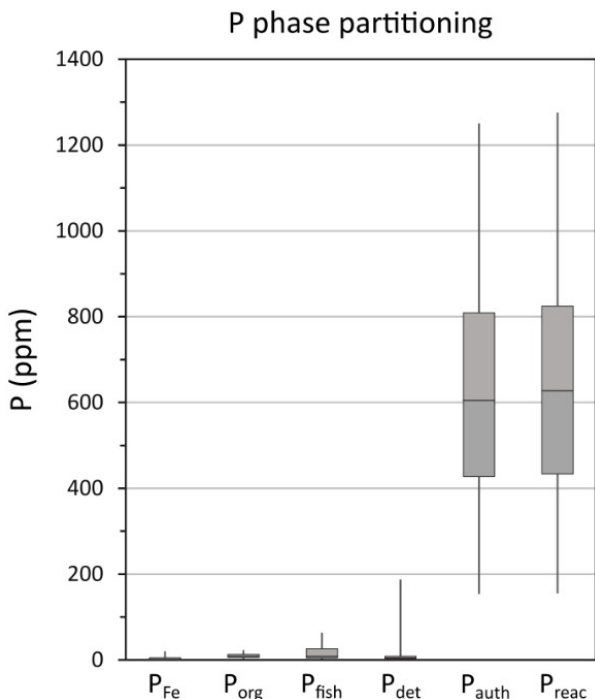
Figure 6. Phase partitioning of P. Boxes represent the range of the interquartile, while whiskers represent the 5th and 95th percentiles.

positive $\delta^{13}C_{org}$ isotope excursion at ~37.9–37.7 m depth (figs. 2 and 5).

Molar C_{org}/P_{reac} ratios are relatively stable in the lower part of the section (on average 500 ± 119), but higher variability occurs above ~40.13 m, with ratios ranging between 61 and 511 (fig. 5). In general, an overall decreasing trend in C_{org}/P_{reac} is apparent towards the top of the core. However, it is also worth noting trends in C_{org}/P_{reac} ratios across the three intervals of particularly high carbonate content (>85% $CaCO_3$) that occur between 37.87–38.37 m prior to the onset of the Holywell Event (HW; see below), 39.96–40.12 m and 41.19–41.32 m core depth (fig. 2). In the lowest carbonate-rich interval, which occurs during the latest stages of phase B when $\delta^{13}C_{org}$ values are still high (fig. 2), C_{org}/P_{reac} ratios (434 ± 81) are relatively high and indistinct from the surrounding background ratios (fig. 5). By contrast, in the middle carbonate-rich interval, which occurs as $\delta^{13}C_{org}$ values start to slightly decrease, C_{org}/P_{reac} ratios drop to lower values (263 ± 70), while in the upper carbonate-rich interval towards the end of the recovery phase, C_{org}/P_{reac} ratios drop further, to values (110 ± 24) close to the Redfield Ratio (fig. 5).

6. DISCUSSION

6.1. Carbon-Sulfur Systematics

The high C_{org} contents that occur throughout most of phase C (up until ~38.50 m depth) indicate that high OM export was maintained in this region, despite the global recovery from the $\delta^{13}C_{org}$ excursion. The decline in $\delta^{13}C_{org}$ reflects the return to pre-OAE conditions, and thus the recovery from the carbon cycle perturbation on a global scale (Arthur et al., 1988), which in other, less productive sites occurs alongside a decrease in C_{org} concentrations (Eldrett et al., 2014; Gangl et al., 2019; van Bentum et al., 2009; van Helmond et al., 2014). The two short positive $\delta^{13}C_{org}$ ex-

cursions between 38.15 and 37.69 m depth appear to represent perturbations to the system during the final stages of the recovery phase. While the first of these excursions has not been documented in other OAE2 locations, the second excursion equates to the Holywell Event, which was first documented by Jarvis et al. (2006) as a small CIE of 0.2‰ in Holywell Chalk. This positive $\delta^{13}C_{org}$ excursion has since been recognized globally, with isotopic shifts varying between 0.5 and 2.5‰ (Gale et al., 2005; Hetzel et al., 2009; van Bentum et al., 2009; van Helmond et al., 2014; Voigt et al., 2008). In the Tarfaya section, a shift of ~2.5‰ is apparent, which is similar to that observed at the peak of the C cycle perturbation in phase B (fig. 2).

The molar ratio of Fe_{HR}:S is consistently below the 1:2 ratio of Fe:S in pyrite (fig. S3), which is the main removal mechanism for sulfate under anoxic marine conditions (Poulton & Canfield, 2011), indicating an overall excess of S over Fe. This occurs despite elevated Fe_{py}/Fe_{HR} ratios, suggesting that the system was likely reactive iron-limited and hence the redox conditions were not controlled by highly elevated riverine Fe inputs (c.f. Scholz et al., 2019). This observation is supported by the high degree of OM sulfurization, where S is overwhelmingly in the form of S_{org}, rather than as pyrite-S, with S_{org} showing a similar profile to C_{org} (figs. 2 and S4). Rapid, particle-hosted sulfurization of OM under oxygen-depleted conditions has been considered to play a key role in enhancing the preservation of C_{org} during OAEs (Hülse et al., 2019; Raven et al., 2019) and in particular in the Tarfaya basin (Kolonic et al., 2005).

6.2. Water Column Redox Conditions

Despite the occasional occurrence of limited bioturbation, the redox proxy results show consistently elevated values, probably because bioturbation during short-term intervals of oxygenation would homogenise the sediment over the affected sample depths (2–6 cm), maintaining overall enrichments in Fe_{HR} and RSTE (Poulton, 2021). Elevated Fe_{HR}/Fe_T ratios (>0.38) and U_{EF}^* values (>5) are entirely consistent with near-persistent bottom water anoxia throughout the section (fig. 3). In support of this, a negative correlation is apparent between U and $CaCO_3$ contents (R=0.73, fig. S5), indicating that U patterns are not controlled by incorporation into carbonate phases (Sturchio et al., 1998; Zhao et al., 2016), and instead likely represent authigenic enrichments due to persistent anoxia. Furthermore, Fe_T concentrations show high variability within the carbonate-rich layers (fig. 2 and fig. S6) and Fe_{HR}/Fe_T ratios show no systematic changes related to lithology (fig. 3), suggesting an independent control driven by water column anoxia.

Euxinic water column conditions of variable intensity are indicated by high Fe_{py}/Fe_{HR} ratios and highly elevated, but variable, Mo_{EF}^* values (fig. 3). However, it remains possible that the water column may have periodically fluctuated to ferruginous conditions, but with elevated Mo drawdown occurring due to the presence of sulfidic porewaters at the sediment-water interface (Goldberg et al., 2016; Poulton et al., 2015). The ultimate phase that sequestered Mo is unclear, but the high concentrations of S_{org} (fig. 2),

alongside the strong relationships between both C_{org} and Mo, and S_{org} and Mo (fig. 4), suggest that sulfurized OM may have been a major host (Kolonic et al., 2002; Tribovillard et al., 2004). However, when considered in detail, it is apparent that the observed variability in Mo_{EF}^* values is not solely due to changes in C_{org}, since there are clear intervals of decoupled behaviour, including, for example, between strongly euxinic intervals E2 and E3, when Mo_{EF}^* values decrease as C_{org} increases (fig. 3). Thus, the variability in Mo_{EF}^* values more likely reflects changes in the intensity of euxinia, which itself may at least partly reflect productivity levels and the intensity of C_{org} production in the water column, which would produce the overall correlation observed between C_{org} and Mo (fig. 4).

In total, 9 moderately to strongly euxinic intervals may be identified by relative variability in Mo_{EF}^* values (fig. 3; note that the temporal extent of interval E9 is based on additional considerations discussed below). In the lower part of the section (below ~38.9 m), intervals E1-E5 have particularly high Mo_{EF}^* values. However, while clear peaks in Mo_{EF}^* values are apparent in this part of the section, peaks E1-E2 and E3-E5 appear to cluster across two broader intervals of generally more intense euxinia (fig. 3). It is interesting to note that these two broader intervals appear to repeat on a timescale that is similar to the clear cyclicity that occurs between euxinic and ferruginous conditions during phase A of OAE2 at Tarfaya (Poulton et al., 2015), although our data suggest fluctuations in the intensity of euxinia during the final stages of phase B, rather than clear transitions to ferruginous conditions.

Above ~39.0 m depth, a clear feature is a progressive decrease in Mo_{EF}^* values from E6 to E9. Although Mo depletion has been suggested for phase A of OAE2, due to global drawdown of Mo under extensive euxinia (Eldrett et al., 2014; Goldberg et al., 2016; Hetzel et al., 2009; Ostrander et al., 2017; Owens et al., 2013), such a process seems unlikely to have become more prevalent during the recovery phase. The exception to this relates to the HW. Here, the global $\delta^{13}C_{org}$ perturbation (fig. 2) likely indicates a return to more reducing conditions on a widespread scale, which is supported by evidence for more intense euxinia at Tarfaya based on both P systematics (see discussion below) and a clear spike in U_{EF}^* values (fig. 3). Thus, the relatively low Mo_{EF}^* values apparent during the HW likely result from global Mo drawdown due to expanded global euxinia, which finds support in observations of Mo enrichments at the beginning of this event at other sites, which are then followed by Mo depletion (Hetzel et al., 2009; van Bentum et al., 2009; van Helmond et al., 2014). This is also consistent with a return to higher Mo_{EF}^* values above the HW interval (fig. 3), where the $\delta^{13}C_{org}$ profile documents the end of OAE2 on a global scale (fig. 1), suggesting that the higher Mo_{EF}^* values likely reflect local euxinia and a replenishment of the global Mo reservoir under more pervasively oxygenated conditions.

Overall, the progressively diminished Mo enrichments apparent during the recovery phase appear to document gradually decreasing dissolved sulfide concentrations. Indeed, it is notable that the cyclical fluctuations become par-

ticularly pronounced as the recovery phase of the OAE proceeds (as indicated by the onset of a more rapid recovery in the $\delta^{13}C_{org}$ profile at ~39 m; fig. 2), and we explore potential controls on these dynamic redox fluctuations below.

6.3. Phosphorus Cycling

Changes in P_T concentrations and P_T/Al ratios show no consistent relationship to the intensity of euxinia (fig. 7), but the P_T profile is broadly similar to the C_{org} profile, which perhaps unsurprisingly suggests that C_{org} was the dominant phase that delivered P to the sediment, rather than drawdown in carbonate phases (see Poulton & Canfield, 2006). However, given that C_{org} contents are relatively high (fig. 5), the low P_{org} values apparent throughout the studied interval (fig. 6), which also occur during phases A and B at Tarfaya (Kraal et al., 2010), imply extensive preferential release of P from OM during early diagenesis (Ingall & Jahnke, 1997). This is supported by the exceptionally high molar C_{org}/P_{org} ratios that occur throughout the studied interval (fig. 5). In addition, however, the progressive decrease observed in C_{org}/P_{org} ratios (excluding the clear spike during the HW; fig. 5) is entirely consistent with the evidence from Mo_{EF}^{*} values for an overall decrease in the intensity of sulfide production (fig. 3). Superimposed on this trend, there are slight peaks in C_{org}/P_{org} ratios during some of the intervals identified as being characterised by more intense euxinia (for example, E1-E2, E6, E7, and particularly E9), which is also consistent with a microbial sulfate reduction control on the preferential release of P from OM.

The occurrence of considerably lower molar C_{org}/P_{reac} ratios relative to molar C_{org}/P_{org} ratios (fig. 5) clearly demonstrates sink switching of a large proportion of the P released from OM, with the P dominantly being fixed in the form of authigenic carbonate fluorapatite (fig. 6). However, throughout much of the section, the elevated C_{org}/P_{reac} ratios relative to the Redfield Ratio demonstrate extensive recycling of a proportion of the released P back to the water column (fig. 5). In this relatively shallow water setting, this recycled P would have imposed a positive productivity feedback (Van Cappellen & Ingall, 1994), thus helping to maintain high levels of OM production and burial, as well as anoxic water column conditions.

There is, however, a suggestion of an overall progressive decrease (and more variability) in P recycling in the upper half of the section, including intervals where C_{org}/P_{reac} ratios are close to the Redfield Ratio (fig. 5). Sedimentation rate may impact the extent of P recycling, and it is noticeable that the particularly low C_{org}/P_{reac} ratios that occur from 38.37–37.87 m coincide with an interval of very high carbonate content, potentially reflecting more rapid sedimentation and hence more efficient trapping of P in the sediment. However, the progressive decrease in C_{org}/P_{reac} ratios that occurs across the three intervals of particularly high carbonate deposition identified above, supports a general decrease in the intensity of P recycling through the recovery phase. This is again consistent with the proposed decrease in both the production of sulfide and the preferential release of P from OM. It is also noticeable that there

are peaks in P within the upper carbonate-rich interval (indicated by elevated P_T/Al ratios at ~38.27 m and ~38.09 m) that do not coincide with elevated C_{org}, suggesting particularly enhanced sequestration of P in the sediment (fig. 5). Thus, while P recycling was a pervasive feature throughout most of OAE2 (Beil et al., 2020; Kraal et al., 2010; Mort et al., 2007, 2008; Poulton et al., 2015), including during much of the recovery phase, the overall decrease in recycling towards the end of the recovery phase likely points to a driving mechanism for the termination of water column anoxia through decreased P availability.

The HW represents an interruption to this general trend, whereby C_{org}/P_{reac} ratios increase substantially, despite continued deposition of sediments with a very high carbonate content (c.f. figs. 2 and 5). This is consistent with more intense P recycling back to the water column due to a return to more intense euxinia. This, in turn, likely resulted in the higher C_{org} contents of the HW interval (up to 3.8 wt%; fig. 5) relative to the background contents (1.1 ± 0.6 wt%) of the preceding carbonate-rich horizon.

6.4. Controls on Redox Cycling

Having established a strong redox control on P cycling, we next consider possible drivers of the observed redox changes, as well as reasons for the distinctive dynamics of the recovery phase relative to the end of phase B. Poulton et al. (2015) argued that the redox cyclicity observed during phase A of OAE2 was due to fluctuations in the relative weathering influxes of sulfate and reactive Fe, reflecting orbitally-driven perturbations to the hydrological cycle. In a setting such as Tarfaya, an alternative possibility relates to changes in the availability of dissolved sulfate due to extensive drawdown (as pyrite) under euxinic conditions. We investigate these possibilities via an integrated consideration of several pertinent aspects of the data.

The isotopic composition of Cretaceous seawater sulfate is considered to have been relatively heterogeneous (in the range of ~8–22‰), with values of 18–19‰ generally occurring towards the end of OAE2 (Adams et al., 2010; Owens et al., 2013; Paytan et al., 2004; Poulton et al., 2015). This gives fractionations between seawater sulfate and $\delta^{34}S_{py}$ of 40–50‰ in the lower part of our section (below ~40 m), which are atypical of Mesozoic fractionations as a whole, and instead are similar to those commonly observed during the lower Paleozoic, when seawater sulfate concentrations are considered to have been lower than average Mesozoic concentrations (Algeo et al., 2015). These fractionations are, however, consistent with the suggestion of relatively low seawater sulfate concentrations (estimated to be in the range of <1 to ~7 mM) during OAE2 itself Adams et al., 2010; Gomes et al., 2016; Owens et al., 2013; Poulton et al., 2015). Such low background concentrations would potentially promote significant changes in seawater sulfate concentrations as a consequence of intense euxinia, and hence ultimate drawdown of sulfate (via sulfide) as pyrite.

Changes in sulfate availability would also have had an impact on the $\delta^{34}S$ signature of sulfurized OM. However, while $\delta^{34}S_{py}$ fluctuations are observed throughout OAE2 in Tarfaya, the $\delta^{34}S$ composition of S_{org} remains relatively
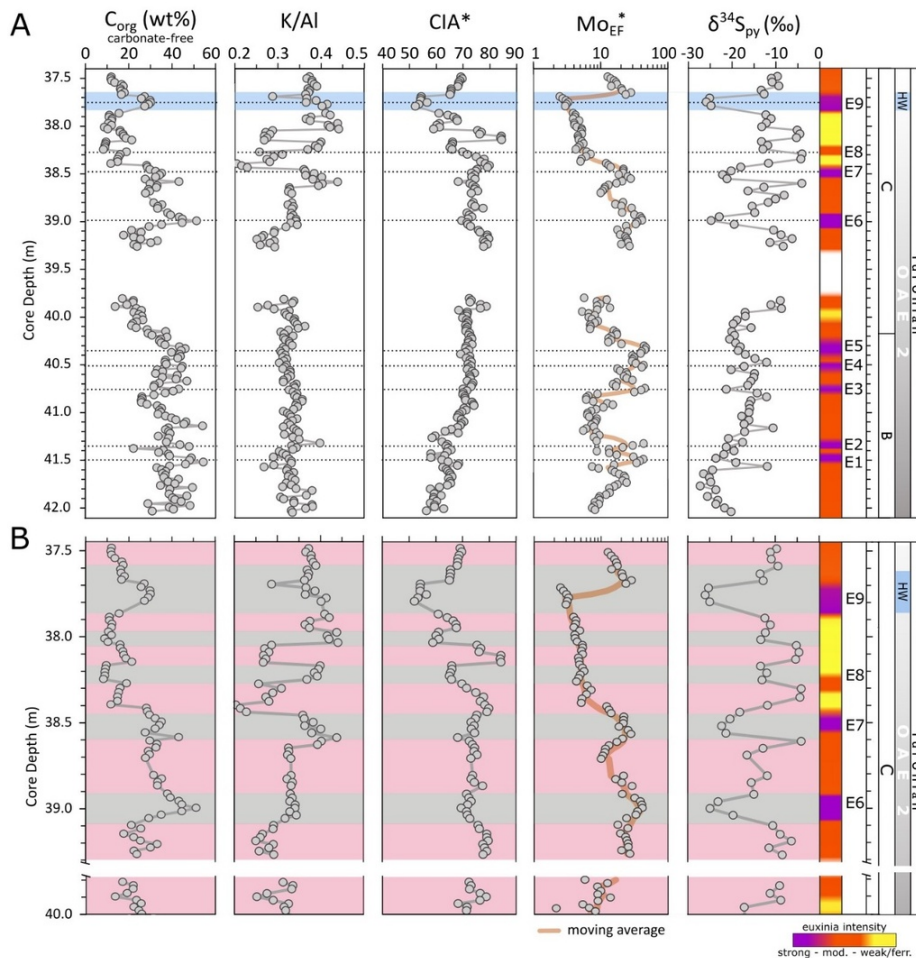
Figure 7. Depth profiles for C_{org} on a carbonate-free basis, K/Al ratios and CIA*, Mo_{EF}* values and $\delta^{34}S_{py}$. (A) Complete analyzed section. (B) Expanded view of the upper part of the analyzed section. Grey bars broadly represent a combination of generally lower intensity of chemical weathering, more intense euxinia and lower $\delta^{34}S_{py}$, while pink bars represent generally higher chemical weathering (which is particularly apparent from redox zone E7 onwards), less intense euxinia and higher $\delta^{34}S_{py}$. Colored bar for redox conditions as in fig. 3.

stable (Raven et al., 2019), suggesting that changes in seawater sulfate concentrations were unlikely to have been the dominant driver for the observed isotopic shifts in $\delta^{34}S_{py}$. However, in addition to being influenced by sulfate availability in the water column, $\delta^{34}S_{py}$ fractionations may also be controlled by sedimentation rate (which affects the extent of pyrite formation under closed system conditions during diagenesis) and C_{org} loading (for example, W. Chen et al., 2022; Liu et al., 2021; Pasquier et al., 2017; Pasquier, Bryant, et al., 2021; Pasquier, Fike, et al., 2021). Thus, we consider these possibilities in terms of the $\delta^{34}S_{py}$ record through the studied interval.

In the lower half of the section (up to a depth of ~40 m), the $\delta^{34}S_{py}$ record shows no distinct trend in relation to the suggested redox variability (which is similar to phase A at Tarfaya; Poulton et al., 2015), but there is an overall increase in $\delta^{34}S_{py}$ values up-section (fig. 7). It is difficult to conclusively resolve the underlying reason for this increase, but a slight increase in sedimentation rate has been proposed between the end of phase B and the beginning of phase C (Kolonic et al., 2005). While the low resolution of the sedimentation rate reconstruction precludes a direct

comparison with the $\delta^{34}S_{py}$ profile, if the suggested higher sedimentation rate was progressive, it may have contributed to the overall increase in $\delta^{34}S_{py}$ by increasingly focusing the locus of pyrite formation deeper in the sediments (Liu et al., 2021; Pasquier, Bryant, et al., 2021; Pasquier et al., 2017; Pasquier, Fike, et al., 2021). In this scenario, increased sedimentation rates would have limited the diffusion of sulfate into the sediment, thereby increasing $\delta^{34}S_{py}$ compositions. By contrast, there is no evidence for consistent changes in C_{org} export, either when reported in terms of bulk contents (fig. 2) or on a carbonate-free basis (fig. 7). Together with the persistently high C_{org} contents, this suggests that changes in C_{org} availability did not drive the observed trend in $\delta^{34}S_{py}$ below ~40 m depth.

Above a depth of ~40 m there is a change in the nature of the $\delta^{34}S_{py}$ signal, with clear cyclicity between higher and lower values (fig. 7). Again, these cycles show no consistency with C_{org} contents (figs. 2 and 7), and we also note that there is no evidence for linked changes in sedimentation rate that could otherwise drive changes in $\delta^{34}S_{py}$. Indeed, fluctuations in the extent of carbonate deposition, which may reflect changes in sedimentation rate, are en-

tirely independent of the observed cyclicity in $\delta^{34}S_{py}$ (figs. 2 and 7). However, other parameters do show broadly consistent behaviour (fig. 7B), although the degree of consistency shows some variability. Above a depth of ~40 m, higher $\delta^{34}S_{py}$ values commonly coincide with intervals of lower Mo_{EF}^* values (i.e., less intense euxinia) and vice versa (noting the discussion above about decreased Mo_{EF}^* values through interval E9) (fig. 7B). This observation is inconsistent with a water column sulfate concentration control on the redox cyclicity. If this were the case, intervals of intense euxinia should have promoted decreased sulfate availability and hence higher $\delta^{34}S_{py}$ compositions, which is opposite to the observed trends. As an alternative, integrated explanation for the observed changes in redox conditions and $\delta^{34}S_{py}$ systematics through the section, we thus consider potential weathering controls using CIA* and K/Al ratios.

Similar to the $\delta^{34}S_{py}$ profile, CIA* values show a slight overall increase up to a depth of ~40 m, with no distinct relationship to the observed redox variability (fig. 7A). Similarly, K/Al ratios show no relationship to the redox variability (fig. 7A). These weathering proxy profiles thus suggest a slight increase in the intensity of chemical weathering towards the end of phase B, which is consistent with peak temperatures occurring at the C/T boundary (Hasegawa et al., 2012; Lunt et al., 2016; O'Brien et al., 2017). Overall, the weathering signal is muted in the lower part of the section. A similar muted continental weathering signal has been reported for OAE2 in the WIS (Nana Yobo et al., 2021). Here, both Sr and Os isotopes show a typical hydrothermal signature at the beginning of OAE2 related to increased volcanic activity, while an effect of continental weathering on the Sr influx is not apparent. However, due to the proximity of the WIS to the Caribbean LIP emplacement, changes in continental input may have been masked by the increased volcanic Sr supply. During the course of OAE2, the Sr weathering signal becomes more prominent, likely due to waning volcanism (see below).

As phase C progresses, there are much clearer relationships between $\delta^{34}S_{py}$, the intensity of euxinia, and chemical weathering intensity, with variability in the weathering proxies becoming increasingly pronounced (fig. 7B). Our data demonstrate that the intervals of more intense euxinia and lower $\delta^{34}S_{py}$ generally correspond to intervals of decreased weathering intensity (i.e., higher K/Al ratios and lower CIA* values). Higher rates of chemical weathering tend to increase the oceanic influxes of both sulfate and Fe_{HR}, as a result of increased pyrite weathering (Poulton & Canfield, 2011). However, the influx of Fe_{HR} is increased relative to sulfate, because in addition to being sourced from the oxidation of pyrite, more intense chemical weathering converts more silicate Fe to Fe_{HR} (Canfield, 1997; Poulton & Raiswell, 2002). Thus, more intense weathering results in a higher Fe_{HR}:sulfate ratio.

The modern ocean is poised at a molar Fe_{HR}:sulfate ratio of 1:1.8, which is close to the stoichiometric 1:2 ratio of Fe_{HR} and sulfide in pyrite (Poulton & Canfield, 2011). Since the dominant initial removal mechanism for Fe_{HR} and sulfate on a global scale is generally in the form of pyrite in anoxic settings, a riverine input with a higher Fe_{HR}:sulfate ratio would promote lower sulfide availability in the water column due to more intense scavenging by Fe_{HR} (Poulton et al., 2015). Indeed, the Tarfaya region would have been particularly prone to changes in sulfide availability through the additional intensive drawdown of sulfide in association with OM (i.e., as S_{org}; fig. 2). Overall, more intense chemical weathering would have resulted in less intense water column euxinia, or even the development of ferruginous conditions (Poulton & Canfield, 2011), as evident during phase A at Tarfaya (Poulton et al., 2015). The higher availability of Fe_{HR} would also have shifted the dominant locus of pyrite formation to deeper in the sediments, where under closed system conditions (with respect to sulfate diffusion into the sediment porewaters), increased $\delta^{34}S_{py}$ compositions would have been generated, as observed in the record at Tarfaya (fig. 7).

Conversely, lower intensity chemical weathering would have resulted in relatively more intense euxinia as less sulfide would have been scavenged by Fe_{HR} in the water column. Furthermore, since rates of sulfidation of Fe_{HR} depend on ambient sulfide concentrations (Canfield et al., 1992; Poulton et al., 2004), higher sulfide concentrations in the water column would have led to proportionately more Fe_{HR} being sulfidized, either directly in the water column or during very early diagenesis when porewaters were still open to diffusion of sulfate from the water column (Meyers, 2007; Poulton et al., 2015). This more open system $\delta^{34}S_{py}$ scenario would have resulted in the observed lighter $\delta^{34}S_{py}$ compositions relative to intervals of more intense chemical weathering and lower sulfide concentrations (fig. 7).

In summary, and consistent with recent studies of pyrite-S isotope systematics (for example, Bryant et al., 2020; Liu et al., 2021; Pasquier, Bryant, et al., 2021; Pasquier et al., 2017; Raven et al., 2019), our $\delta^{34}S_{py}$ data do not simply reflect changes in water column sulfate availability, but rather reflect a balance between the relative significance of "early" (water column/shallow sediment) versus "late" (deeper in the sediment) pyrite formation. However, rather than being driven by changes in sedimentation rate or C_{org} loading, our data suggest that under anoxic conditions, the intensity of water column euxinia (which was influenced by the relative availability of Fe_{HR}) likely exerted a major control on the observed shifts in $\delta^{34}S_{py}$. Furthermore, while a variety of factors may have contributed (see fig. 8), changes in the intensity of chemical weathering appear to have exerted a dominant control on the observed redox variability by altering the Fe_{HR}:sulfate ratio in the basin (and hence the extent of P recycling). In the upper part of the section, the redox variability was likely driven by orbital-timescale changes in the hydrological cycle (Wagner et al., 2013), as previously suggested for phase A at Tarfaya (Poulton et al., 2015). In the lower part of the section, the progressive increase in $\delta^{34}S_{py}$ also appears to have been affected by a slight increase in chemical weathering intensity as phase B came to an end, although a potential increase in sedimentation rate may also have contributed.
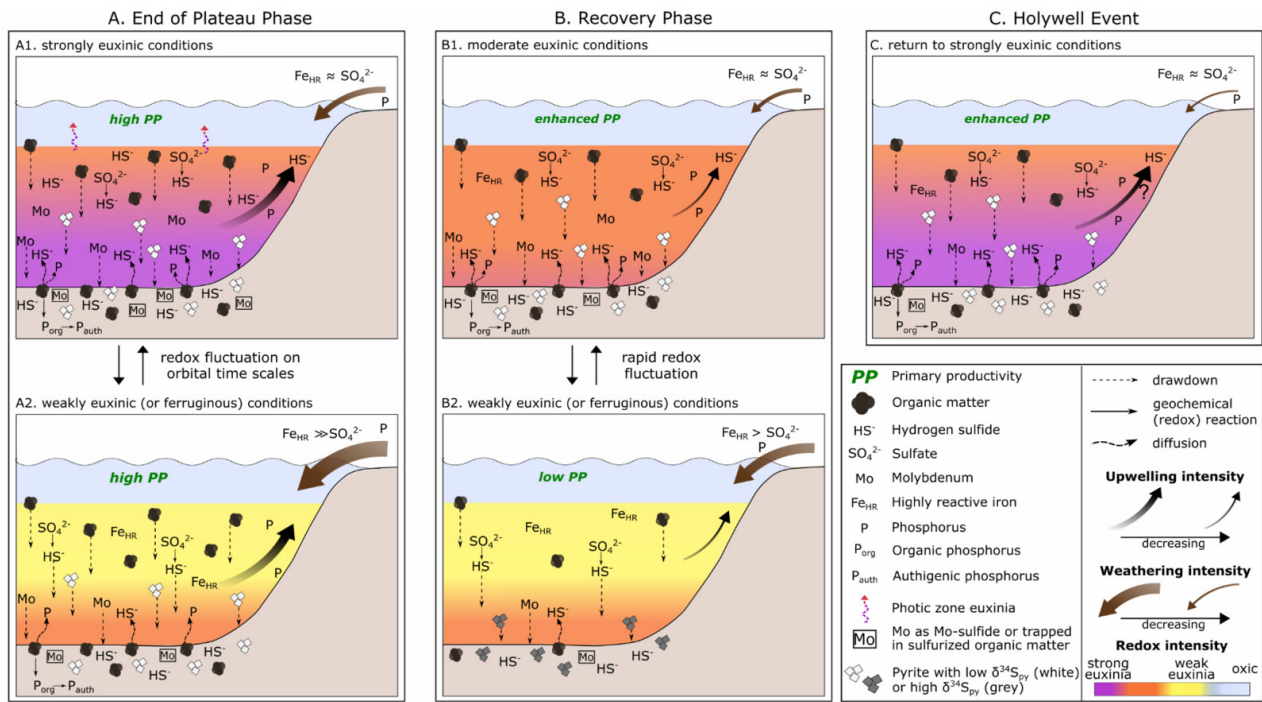
Figure 8. Simplified depositional model for the shallow Tarfaya shelf, showing the development from the end of the plateau phase (A) to the recovery phase (B), and the short-term perturbation during the Holywell Event (C).

An additional interesting feature of the data concerns the muted response of weathering parameters and $\delta^{34}S_{py}$ values to orbital forcing during the end of the OAE2 phase B, relative to the phase A and phase C. We suggest that this may be due to the relative significance of orbital changes in the hydrological cycle and chemical weathering at times of peak temperatures, compared to the onset and termination of such climatic perturbations. As mentioned above, peak temperatures are considered to have occurred around the C/T boundary (i.e., at the end of the phase B; Hasegawa et al., 2012; Lunt et al., 2016; O'Brien et al., 2017), and indeed, OAE2 is considered to represent one of the warmest intervals of the Phanerozoic (Jenkyns, 2010). Particularly high temperatures at high latitudes would have resulted in a low temperature gradient between the poles and the equator (Barron, 1983). We thus speculate that at these extreme temperatures, the effects of orbital forcing on the hydrological cycle and hence weathering intensity would have been more muted. Indeed, a nonlinear response of both the sedimentary record and the hydrological cycle to orbital forcing, in particular at low latitudes, has been shown in climate modeling (Park & Oglesby, 1991). Nevertheless, despite the muted response evident at Tarfaya, orbital forcing does appear to have had a more subtle influence on the intensity of euxinia during the end of phase B, as indicated by the two clusters (for example, E1-E2 and E3-E5) of more intense euxinia (fig. 3).

6.5. Controls on the Termination of OAE2

The general driver behind the termination of OAE2 is considered to have been a return to cooler temperatures and a less active hydrological cycle as a result of CO_2 sequestration through both silicate weathering and the burial of OM (Arthur et al., 1988; Hülse et al., 2019; Kuypers et al., 1999), which is supported by various weathering proxies (Pogge von Strandmann et al., 2013). Ultimately, this would have exerted a negative feedback on chemical weathering and the oceanic influx of nutrients, thus impacting global rates of productivity and carbon production, and hence water column oxygen depletion (Pogge von Strandmann et al., 2013). Tracers for weathering intensity such as Li isotopes, Sr isotopes and Hf isotopes, reported for the Tethys (Frijia & Parente, 2008; Pogge von Strandmann et al., 2013) and at high-latitudes in both the proto-Indian Ocean (H. Chen et al., 2023; Jones et al., 2023) and the Pacific Ocean (Takashima et al., 2024), show a 1.8- to 3.0-fold increase in chemical weathering (Jones et al., 2023; Nana Yobo et al., 2021; Pogge von Strandmann et al., 2013) coincident with the onset of OAE2. While the timing and intensity of the weathering perturbation does not seem to be uniform (Blättler et al., 2011; Pogge von Strandmann et al., 2013), weathering proxies across all locations report a decrease in weathering intensity towards the end of the CIE recovery phase (Blättler et al., 2011; H. Chen et al., 2023; Jones et al., 2023; Pogge von Strandmann et al., 2013; Takashima et al., 2024).

These observations are consistent with our findings. An overall decrease in chemical weathering intensity through phase C is supported by our CIA* and K/Al profiles, where, despite the evident cyclicity, background CIA* values progressively decrease, and K/Al ratios progressively increase (fig. 7). While this would have impacted the weathering supply of nutrients to the basin (fig. 8A and B), we also note that Tarfaya was located within the outer limb of the Hadley Cell, where trade wind intensities are closely linked

to latitudinal variations in the position of the Intertropical Convergence Zone (ITCZ; Wagner et al., 2013). It has been proposed that an interplay between trade wind induced upwelling and the collapse of the upwelling cell occurred during the termination of OAE2 (Kolonic et al., 2005; Prauss, 2012). Thus, although anoxia was maintained at Tarfaya, at least during phase C of OAE2 (fig. 3), the total supply of nutrients to the Tarfaya basin may have been significantly reduced as a consequence of both decreased chemical weathering influxes and decreased upwelling (fig. 8B).

In addition, model simulations have shown that rapid sulfurization of OM results in enhanced C_{org} preservation in sediments (Hülse et al., 2019), which would draw down CO_2 and lower rates of oxygen consumption in the water column. As discussed above, sulfurization of OM would help to remove dissolved sulfide from the water column. Thus, the combined effects of OM sulfurization would help the recovery from strongly euxinic conditions (Hülse et al., 2019). However, while decreased nutrient fluxes and sulfurization of OM likely set the stage for the recovery from extreme redox conditions, our high-resolution data provide nuanced insight into the dynamics and precise nature of the processes that allowed the ocean to recover from the global OAE2 perturbation (fig. 8).

During the recovery period (fig. 8B), euxinia became progressively less intense (with the exception of the HW), which was likely initiated by the proposed decrease in the supply of nutrients. In addition, stronger fluctuations between weak and more intense euxinia are apparent, relative to the phase B (fig. 8A), and these fluctuations became more frequent during phase C (fig. 7). This resulted in a progressive decrease in P remobilisation from OM during diagenesis, as indicated by decreased C_{org}/P_{org} ratios, as well as intervals of greatly reduced P recycling back to the water column, as indicated by low C_{org}/P_{reac} ratios (fig. 5). Indeed, there are intervals where C_{org}/P_{reac} ratios sit close to, or below, the Redfield Ratio (fig. 5). In a persistently anoxic setting such as Tarfaya, C_{org}/P_{reac} ratios below the Redfield Ratio suggest additional drawdown of P in association with Fe (oxyhydr)oxide minerals that escaped sulfidation in the euxinic water column (for example, Alcott et al., 2022; Bowyer et al., 2020; Guilbaud et al., 2020), with sink switching of P_{Fe} to P_{auth} during the reductive dissolution of Fe (oxyhydr)oxides during diagenesis. This process would have actively created a negative productivity feedback, further aiding the recovery from intensely reducing conditions.

Although similar detailed studies of other shelf, and particularly deeper water, settings are required, our data suggest that decreased recycling of P from shelf environments, coupled with waning nutrient influxes from continental weathering, likely drove the recovery from global anoxia. This recovery persisted over a protracted period during which orbitally-driven changes in the intensity of euxinia impacted the efficiency of P sequestration in the sediments. This is particularly apparent during the HW (fig. 8C), when the ocean appears to have returned to a more reduced state on a global scale, as indicated by the global $\delta^{13}C_{org}$ excursion. At Tarfaya, the HW is characterized by a particularly low chemical weathering input (fig. 7B), which we suggest initiated a biogeochemical cascade, starting with a reduced input of Fe_{HR} relative to sulfate and leading to more intense water column euxinia (fig. 5). This subsequently promoted efficient P recycling back to the water column (fig. 8C), driving enhanced primary productivity not only on the Tarfaya shelf, but also probably in the global ocean (likely with differing degrees of impact in different regions), as indicated by the global, but variable (in terms of magnitude) nature of the HW $\delta^{13}C_{org}$ excursion.

It is also interesting to note that a global short-term perturbation is observed shortly after the *initiation* of OAE2, where a sharp overall increase in $\delta^{13}C_{org}$ is interrupted by the Plenus Cold Event (PCE; Forster et al., 2007; Gale & Christensen, 1996; Jefferies, 1962), represented by a negative isotopic shift of 1–2‰ that divides the onset of the CIE into two phases (fig. 1D). Intermittent cooling during the PCE (Lamolda et al., 1994; Sinninghe Damsté et al., 2010) has been interpreted to be a direct consequence of extensive removal of atmospheric CO_2 (Jarvis et al., 2011; Kuypers et al., 1999). While the PCE is represented globally in the geological record, concomitant cooling during the PCE is not consistent in timing and expression (O'Connor et al., 2020). For the HW, global temperature reconstructions suggest relatively warm, stable sea surface temperatures lasting until the mid-Turonian, with no particular changes during the HW itself, although the resolution of these studies may have been insufficient to document such a short-lived change (Forster et al., 2007; Robinson et al., 2019). Similar to the PCE, the HW does not seem to show consistency on a global scale. Nevertheless, both the HW and the PCE document environmental instability as the Earth system transitioned from one climate state to another, and hence it is intriguing to consider that such instability may be a common feature during the transition stages of major climate-induced perturbations.

7. CONCLUSIONS

Our high-resolution geochemical study of the mid-Cretaceous, high-productivity Tarfaya shelf documents persistent anoxia, with fluctuations in the intensity of euxinia, from the end of phase B of OAE2 and through phase C. Towards the end of phase B, intervals of intense euxinia repeat on a timescale similar to the redox cyclicity that is apparent during phase A of OAE2. However, during the recovery period, fluctuations in the intensity of euxinia became more pronounced and more rapid. In addition, the intensity of euxinia progressively decreased during phase C, with the exception of a return to particularly intense euxinia during the global Holywell Event.

Consideration of chemical weathering proxies (CIA*, K/Al) suggests a relatively muted response to orbital forcing of the hydrological cycle towards the end of phase B, although this may still have driven the observed, relatively subtle changes in the intensity of euxinia. During phase C, intervals of enhanced chemical weathering clearly coincide with less intense euxinia. Consistent with phase A at Tarfaya (Poulton et al., 2015), we suggest that this reflects an

enhanced influx of Fe_{HR} relative to sulfate from land, due to the increased transfer of unreactive silicate Fe to Fe_{HR} as weathering intensity increased. A greater availability of Fe_{HR} ultimately promoted less intense euxinia and also resulted in proportionately more Fe_{HR} being sulfidized during diagenesis, which promoted the observed increases in $\delta^{34}S_{py}$.

In general, the prevalence of euxinia led to a high degree of preferential P release during OM remineralization and also extensive P recycling back to the water column, which would have promoted a positive productivity feedback. This helped to maintain exceptionally high levels of OM production at Tarfaya and also may have provided a source of P to maintain widespread ocean anoxia. However, the extent of P recycling progressively diminished as the intensity of euxinia decreased, with intervals of enhanced P drawdown being apparent during phase C. In combination with waning P inputs from chemical weathering, and possibly also a decline in the intensity of P supplied via upwelling, this helped to drive the system to recovery from the C/T boundary carbon cycle perturbation. However, the clear cyclicity apparent in local redox conditions during phase C suggests a high degree of instability, driven by orbital forcing, as the system transitioned from the OAE into a more stable climate state. Global instability during this interval is particularly highlighted by the Holywell Event, where a positive $\delta^{13}C_{org}$ excursion of up to ~2.5‰ interrupts the gradual recovery from the CIE. This short episode of strongly reducing conditions was, perhaps paradoxically, initiated by decreased chemical weathering, which drove the water column to more intense euxinia. Under these conditions, increased P recycling transiently returned, and thus primary productivity was promoted on the shallow Tarfaya shelf, and probably also on a global scale.

In modern oceans, the impact of climate change is visible in the expansion of oxygen minimum zones (Breitburg et al., 2018; Grégoire et al., 2021; Schmidtko et al., 2017). Studies of intervals of past ocean deoxygenation, such as OAE2, clearly show that biogeochemical feedbacks linked to climate change can result in changes in the availability of dissolved sulfide. Linked to this, changes in sulfide availability above a tipping point may lead to extensive recycling of P, thus driving more intense local and global anoxia. In this context, more research is required to identify the precise tipping point(s) and parameters that may drive the ocean system to an extreme reducing condition.

Author contributions

SWP and TW designed the research. Samples were provided by TW. CK performed geochemical analyses. CK and SWP interpreted the data and wrote the manuscript. All authors were involved in the discussion of the project and contributed to revising the manuscript.

Competing Interests

The authors declare no conflict of interests.

Data availability

All the data are available as an electronic supplement.
Supplementary Information: https://doi.org/10.17632/cnjj8smxr3.1
Excel Data: https://doi.org/10.17632/8zdxdbscnf.1

Editor: C. Page Chamberlain, Associate Editor: Kimberly Lau

REFERENCES

Adams, D. D., Hurtgen, M. T., & Sageman, B. B. (2010). Volcanic triggering of a biogeochemical cascade during Oceanic Anoxic Event 2. *Nature Geoscience*, *3*(3), 201–204. https://doi.org/10.1038/Ngeo743

Alcott, L. J., Krause, A. J., Hammarlund, E. U., Bjerrum, C. J., Scholz, F., Xiong, Y., Hobson, A. J., Neve, L., Mills, B. J. W., März, C., Schnetger, B., Bekker, A., & Poulton, S. W. (2020). Development of Iron Speciation Reference Materials for Palaeoredox Analysis. *Geostandards and Geoanalytical Research*, *44*(3), 581–591. https://doi.org/10.1111/ggr.12342

Alcott, L. J., Mills, B. J. W., Bekker, A., & Poulton, S. W. (2022). Earth's Great Oxidation Event facilitated by the rise of sedimentary phosphorus recycling. *Nature Geoscience*, *15*(3), 210–215. https://doi.org/10.1038/s41561-022-00906-5

Algeo, T. J. (2004). Can marine anoxic events draw down the trace element inventory of seawater? *Geology*, *32*(12), 1057–1060. https://doi.org/10.1130/g20896.1

Algeo, T. J., & Ingall, E. (2007). Sedimentary Corg:P ratios, paleocean ventilation, and Phanerozoic atmospheric pO2. *Palaeogeography, Palaeoclimatology, Palaeoecology*, *256*(3–4), 130–155. https://doi.org/10.1016/j.palaeo.2007.02.029

Algeo, T. J., & Li, C. (2020). Redox classification and calibration of redox thresholds in sedimentary systems. *Geochimica Et Cosmochimica Acta*, *287*, 8–26. https://doi.org/10.1016/j.gca.2020.01.055

Algeo, T. J., Luo, G. M., Song, H. Y., Lyons, T. W., & Canfield, D. E. (2015). Reconstruction of secular variation in seawater sulfate concentrations. *Biogeosciences*, *12*(7), 2131–2151. https://doi.org/10.5194/bg-12-2131-2015

Algeo, T. J., & Lyons, T. W. (2006). Mo-total organic carbon covariation in modern anoxic marine environments: Implications for analysis of paleoredox and paleohydrographic conditions. *Paleoceanography*, *21*(1). https://doi.org/10.1029/2004pa001112

Algeo, T. J., & Tribovillard, N. (2009). Environmental analysis of paleoceanographic systems based on molybdenum-uranium covariation. *Chemical Geology*, *268*(3–4), 211–225. https://doi.org/10.1016/j.chemgeo.2009.09.001

Anderson, L. A., & Sarmiento, J. L. (1994). Redfield ratios of remineralization determined by nutrient data analysis. *Global Biogeochemical Cycles*, *8*(1), 65–80. https://doi.org/10.1029/93GB03318

Anderson, L. D., Delaney, M. L., & Faul, K. L. (2001). Carbon to phosphorus ratios in sediments: Implications for nutrient cycling. *Global Biogeochemical Cycles*, *15*(1), 65–79. https://doi.org/10.1029/2000gb001270

Anderson, R. F., Fleisher, M. Q., & LeHuray, A. P. (1989). Concentration, oxidation state, and particulate flux of uranium in the Black Sea. *Geochimica Et Cosmochimica Acta*, *53*(9), 2215–2224. https://doi.org/10.1016/0016-7037(89)90345-1

Anderson, T. F., & Raiswell, R. (2004). Sources and mechanisms for the enrichment of highly reactive iron in euxinic Black Sea sediments. *American Journal of Science*, *304*(3), 203–233. https://doi.org/10.2475/ajs.304.3.203

Arthur, M. A., Dean, W. E., & Pratt, L. M. (1988). Geochemical and climatic effects of increased marine organic carbon burial at the Cenomanian/Turonian boundary. *Nature*, *335*(6192), 714–717. https://doi.org/10.1038/335714a0

Arthur, M. A., Dean, W. E., & Schlanger, S. O. (1985). Variations in the global carbon cycle during the Cretaceous related to climate, volcanism, and changes in atmospheric CO_2. *The Carbon Cycle and Atmospheric CO_2: Natural Variations Archean to Present*, *32*, 504–529. https://doi.org/10.1029/GM032p0504

Arthur, M. A., & Sageman, B. B. (1994). Marine black shales: depositional mechanisms and environments of ancient deposits. *Annual Review of Earth and Planetary Sciences*, *22*(1), 499–551. https://doi.org/10.1146/annurev.ea.22.050194.002435

Arthur, M. A., Schlanger, S. O., & Jenkyns, H. C. (1987). The Cenomanian-Turonian Oceanic Anoxic Event, II. Palaeoceanographic controls on organic-matter production and preservation. *Geological Society, London, Special Publications*, *26*(1), 401–420. https://doi.org/10.1144/gsl.sp.1987.026.01.25

Barron, E. J. (1983). A warm, equable Cretaceous: The nature of the problem. *Earth-Science Reviews*, *19*(4), 305–338. https://doi.org/10.1016/0012-8252(83)90001-6

Beckmann, B., Flögel, S., Hofmann, P., Schulz, M., & Wagner, T. (2005). Orbital forcing of Cretaceous river discharge in tropical Africa and ocean response. *Nature*, *437*(7056), 241–244. https://doi.org/10.1038/nature03976

Beil, S., Kuhnt, W., Holbourn, A., Scholz, F., Oxmann, J., Wallmann, K., Lorenzen, J., Aquit, M., & Chellai, E. H. (2020). Cretaceous oceanic anoxic events prolonged by phosphorus cycle feedbacks. *Climate of the Past*, *16*(2), 757–782. https://doi.org/10.5194/cp-16-757-2020

Benkovitz, A., Matthews, A., Teutsch, N., Poulton, S. W., Bar-Matthews, M., & Almogi-Labin, A. (2020). Tracing water column euxinia in Eastern Mediterranean Sapropels S5 and S7. *Chemical Geology*, *545*, 119627. https://doi.org/10.1016/j.chemgeo.2020.119627

Blättler, C. L., Jenkyns, H. C., Reynard, L. M., & Henderson, G. M. (2011). Significant increases in global weathering during Oceanic Anoxic Events 1a and 2 indicated by calcium isotopes. *Earth and Planetary Science Letters*, *309*(1–2), 77–88. https://doi.org/10.1016/j.epsl.2011.06.029

Bowman, A. R., & Bralower, T. J. (2005). Paleoceanographic significance of high-resolution carbon isotope records across the Cenomanian–Turonian boundary in the Western Interior and New Jersey coastal plain, USA. *Marine Geology*, *217*(3–4), 305–321. https://doi.org/10.1016/j.margeo.2005.02.010

Bowyer, F. T., Shore, A. J., Wood, R. A., Alcott, L. J., Thomas, A. L., Butler, I. B., Curtis, A., Hainanan, S., Curtis-Walcott, S., Penny, A. M., & Poulton, S. W. (2020). Regional nutrient decrease drove redox stabilisation and metazoan diversification in the late Ediacaran Nama Group, Namibia. *Scientific Reports*, *10*(1). https://doi.org/10.1038/s41598-020-59335-2

Breitburg, D., Levin, L. A., Oschlies, A., Grégoire, M., Chavez, F. P., Conley, D. J., Garçon, V., Gilbert, D., Gutiérrez, D., Isensee, K., Jacinto, G. S., Limburg, K. E., Montes, I., Naqvi, S. W. A., Pitcher, G. C., Rabalais, N. N., Roman, M. R., Rose, K. A., Seibel, B. A., & Zhang, J. (2018). Declining oxygen in the global ocean and coastal waters. *Science*, *359*(6371). https://doi.org/10.1126/science.aam7240

Bryant, R. N., Jones, C., Raven, M. R., Owens, J. D., & Fike, D. A. (2020). Shifting modes of iron sulfidization at the onset of OAE-2 drive regional shifts in pyrite δ^{34}S records. *Chemical Geology*, *553*, 119808. https://doi.org/10.1016/j.chemgeo.2020.119808

Canfield, D. E. (1989). Reactive iron in marine sediments. *Geochimica Et Cosmochimica Acta*, *53*(3), 619–632. https://doi.org/10.1016/0016-7037(89)90005-7

Canfield, D. E. (1997). The geochemistry of river particulates from the continental USA: major elements. *Geochimica Et Cosmochimica Acta*, *61*(16), 3349–3365. https://doi.org/10.1016/s0016-7037(97)00172-5

Canfield, D. E., Lyons, T. W., & Raiswell, R. (1996). A model for iron deposition to euxinic Black Sea sediments. *American Journal of Science*, *296*(7), 818–834. https://doi.org/10.2475/ajs.296.7.818

Canfield, D. E., Raiswell, R., & Bottrell, S. H. (1992). The reactivity of sedimentary iron minerals toward sulfide. *American Journal of Science*, *292*(9), 659–683. https://doi.org/10.2475/ajs.292.9.659

Canfield, D. E., Raiswell, R., Westrich, J. T., Reaves, C. M., & Berner, R. A. (1986). The Use of Chromium Reduction in the Analysis of Reduced Inorganic Sulfur in Sediments and Shales. *Chemical Geology*, *54*(1–2), 149–155. https://doi.org/10.1016/0009-2541(86)90078-1

Chen, H., Bayon, G., Xu, Z., & Li, T. (2023). Hafnium isotope evidence for enhanced weatherability at high southern latitudes during Oceanic Anoxic Event 2. *Earth and Planetary Science Letters*, *601*, 117910. https://doi.org/10.1016/j.epsl.2022.117910

Chen, W., Kemp, D. B., Newton, R. J., He, T., Huang, C., Cho, T., & Izumi, K. (2022). Major sulfur cycle perturbations in the Panthalassic Ocean across the Pliensbachian-Toarcian boundary and the Toarcian Oceanic Anoxic Event. *Global and Planetary Change*, *215*, 103884. https://doi.org/10.1016/j.gloplacha.2022.103884

Clarkson, M. O., Poulton, S. W., Guilbaud, R., & Wood, R. A. (2014). Assessing the utility of Fe/Al and Fe-speciation to record water column redox conditions in carbonate-rich sediments. *Chemical Geology*, *382*, 111–122. https://doi.org/10.1016/j.chemgeo.2014.05.031

Dellwig, O., Leipe, T., März, C., Glockzin, M., Pollehne, F., Schnetger, B., Yakushev, E. V., Böttcher, M. E., & Brumsack, H.-J. (2010). A new particulate Mn-Fe-P-shuttle at the redoxcline of anoxic basins. *Geochimica et Cosmochimica Acta*, *74*(24), 7100–7115. https://doi.org/10.1016/j.gca.2010.09.017

Dijkstra, N., Kraal, P., Séguret, M. J. M., Flores, M. R., Gonzalez, S., Rijkenberg, M. J. A., & Slomp, C. P. (2018). Phosphorus dynamics in and below the redoxcline in the Black Sea and implications for phosphorus burial. *Geochimica et Cosmochimica Acta*, *222*, 685–703. https://doi.org/10.1016/j.gca.2017.11.016

Donnadieu, Y., Pucéat, E., Moiroud, M., Guillocheau, F., & Deconinck, J. F. (2016). A better-ventilated ocean triggered by Late Cretaceous changes in continental configuration. *Nature Communications*, *7*(1). https://doi.org/10.1038/ncomms10316

Dummann, W., Hofmann, P., Herrle, J. O., Frank, M., & Wagner, T. (2023). The early opening of the Equatorial Atlantic gateway and the evolution of Cretaceous peak warming. *Geology*, *51*(5), 476–480. https://doi.org/10.1130/G50842.1

Eldrett, J. S., Minisini, D., & Bergman, S. C. (2014). Decoupling of the carbon cycle during Ocean Anoxic Event 2. *Geology*, *42*(7), 567–570. https://doi.org/10.1130/G35520.1

Erickson, B. E., & Helz, G. R. (2000). Molybdenum(VI) speciation in sulfidic waters: Stability and lability of thiomolybdates. *Geochimica Et Cosmochimica Acta*, *64*(7), 1149–1158. https://doi.org/10.1016/S0016-7037(99)00423-8

Fedo, C. M., Wayne Nesbitt, H., & Young, G. M. (1995). Unraveling the effects of potassium metasomatism in sedimentary rocks and paleosols, with implications for paleoweathering conditions and provenance. *Geology*, *23*(10), 921–924. https://doi.org/10.1130/0091-7613(1995)023%3CC0921:UTEOPM%3E2.3.CO;2

Flögel, S., Beckmann, B., Hofmann, P., Bornemann, A., Westerhold, T., Norris, R. D., Dullo, C., & Wagner, T. (2008). Evolution of tropical watersheds and continental hydrology during the Late Cretaceous greenhouse; impact on marine carbon burial and possible implications for the future. *Earth and Planetary Science Letters*, *274*(1–2), 1–13. https://doi.org/10.1016/j.epsl.2008.06.011

Forster, A., Schouten, S., Moriya, K., Wilson, P. A., & Sinninghe Damsté, J. S. (2007). Tropical warming and intermittent cooling during the Cenomanian/Turonian oceanic anoxic event 2: Sea surface temperature records from the equatorial Atlantic. *Paleoceanography*, *22*(1). https://doi.org/10.1029/2006pa001349

Friedrich, O., & Erbacher, J. (2006). Benthic foraminiferal assemblages from Demerara Rise (ODP Leg 207, western tropical Atlantic): possible evidence for a progressive opening of the Equatorial Atlantic Gateway. *Cretaceous Research*, *27*(3), 377–397. https://doi.org/10.1016/j.cretres.2005.07.006

Frijia, G., & Parente, M. (2008). Strontium isotope stratigraphy in the upper Cenomanian shallow-water carbonates of the southern Apennines: Short-term perturbations of marine 87Sr/86Sr during the oceanic anoxic event 2. *Palaeogeography, Palaeoclimatology, Palaeoecology*, *261*(1–2), 15–29. https://doi.org/10.1016/j.palaeo.2008.01.003

Gale, A. S., & Christensen, W. K. (1996). Occurrence of the belemnite Actinocamax plenus in the Cenoinanian of SE France and its significance. *Bulletin of the Geological Society of Denmark*, *43*(1), 68–77. https://doi.org/10.37570/bgsd-1996-43-08

Gale, A. S., Kennedy, W. J., Voigt, S., & Walaszczyk, I. (2005). Stratigraphy of the Upper Cenomanian–Lower Turonian Chalk succession at Eastbourne, Sussex, UK: ammonites, inoceramid bivalves and stable carbon isotopes. *Cretaceous Research*, *26*(3), 460–487. https://doi.org/10.1016/j.cretres.2005.01.006

Gangl, S. K., Moy, C. M., Stirling, C. H., Jenkyns, H. C., Crampton, J. S., Clarkson, M. O., Ohneiser, C., & Porcelli, D. (2019). High-resolution records of Oceanic Anoxic Event 2: Insights into the timing, duration and extent of environmental perturbations from the palaeo-South Pacific Ocean. *Earth and Planetary Science Letters*, *518*, 172–182. https://doi.org/10.1016/j.epsl.2019.04.028

Garzanti, E., Padoan, M., Setti, M., López-Galindo, A., & Villa, I. M. (2014). Provenance versus weathering control on the composition of tropical river mud (southern Africa). *Chemical Geology*, *366*, 61–74. https://doi.org/10.1016/j.chemgeo.2013.12.016

Goldberg, T., Poulton, S. W., Wagner, T., Kolonic, S. F., & Rehkämper, M. (2016). Molybdenum drawdown during Cretaceous Oceanic Anoxic Event 2. *Earth and Planetary Science Letters*, *440*, 81–91. https://doi.org/10.1016/j.epsl.2016.02.006

Gomes, M. L., Hurtgen, M. T., & Sageman, B. B. (2016). Biogeochemical sulfur cycling during Cretaceous oceanic anoxic events: A comparison of OAE1a and OAE2. *Paleoceanography*, *31*(2), 233–251. https://doi.org/10.1002/2015pa002869

Grégoire, M., Garçon, V., Garcia, H., Breitburg, D., Isensee, K., Oschlies, A., Telszewski, M., Barth, A., Bittig, H. C., Carstensen, J., Carval, T., Chai, F., Chavez, F., Conley, D., Coppola, L., Crowe, S., Currie, K., Dai, M., Deflandre, B., & Yasuhara, M. (2021). A Global Ocean Oxygen Database and Atlas for Assessing and Predicting Deoxygenation and Ocean Health in the Open and Coastal Ocean. *Frontiers in Marine Science*, 8. https://doi.org/10.3389/fmars.2021.724913

Guilbaud, R., Poulton, S. W., Thompson, J., Husband, K. F., Zhu, M., Zhou, Y., Shields, G. A., & Lenton, T. M. (2020). Phosphorus-limited conditions in the early Neoproterozoic ocean maintained low levels of atmospheric oxygen. *Nature Geoscience*, *13*(4), 296–301. https://doi.org/10.1038/s41561-020-0548-7

Haq, B. U. (2014). Cretaceous eustasy revisited. *Global and Planetary Change*, *113*, 44–58. https://doi.org/10.1016/j.gloplacha.2013.12.007

Harnois, L. (1988). The CIW index: a new chemical index of weathering. *Sedimentary Geology*, *55*(3–4), 319–322. https://doi.org/10.1016/0037-0738(88)90137-6

Hasegawa, H., Tada, R., Jiang, X., Suganuma, Y., Imsamut, S., Charusiri, P., Ichinnorov, N., & Khand, Y. (2012). Drastic shrinking of the Hadley circulation during the mid-Cretaceous Supergreenhouse. *Climate of the Past*, *8*(4), 1323–1337. https://doi.org/10.5194/cp-8-1323-2012

Helz, G. R., Miller, C. V., Charnock, J. M., Mosselmans, J. F. W., Pattrick, R. A. D., Garner, C. D., & Vaughan, D. J. (1996). Mechanism of molybdenum removal from the sea and its concentration in black shales: EXAFS evidence. *Geochimica Et Cosmochimica Acta*, *60*(19), 3631–3642. https://doi.org/10.1016/0016-7037(96)00195-0

Hetzel, A., Böttcher, M. E., Wortmann, U. G., & Brumsack, H.-J. (2009). Paleo-redox conditions during OAE 2 reflected in Demerara Rise sediment geochemistry (ODP Leg 207). *Palaeogeography, Palaeoclimatology, Palaeoecology*, *273*(3–4), 302–328. https://doi.org/10.1016/j.palaeo.2008.11.005

Huber, B. T., Hodell, D. A., & Hamilton, C. P. (1995). Middle-Late Cretaceous climate of the southern high latitudes: Stable isotopic evidence for minimal equator-to-pole thermal gradients. *Geological Society of America Bulletin*, *107*(10), 1164–1191. https://doi.org/10.1130/0016-7606(1995)107%3C1164:mlccot%3E2.3.co;2

Huber, B. T., Norris, R. D., & MacLeod, K. G. (2002). Deep-sea paleotemperature record of extreme warmth during the Cretaceous. *Geology*, *30*(2), 123–126. https://doi.org/10.1130/0091-7613(2002)030%3C0123:Dsproe%3E2.0.Co;2

Hülse, D., Arndt, S., & Ridgwell, A. (2019). Mitigation of extreme ocean anoxic event conditions by organic matter sulfurization. *Paleoceanography and Paleoclimatology*, *34*(4), 476–489. https://doi.org/10.1029/2018PA003470

Ingall, E., Bustin, R. M., & Van Cappellen, P. (1993). Influence of Water Column Anoxia on the Burial and Preservation of Carbon and Phosphorus in Marine Shales. *Geochimica Et Cosmochimica Acta*, *57*(2), 303–316. https://doi.org/10.1016/0016-7037(93)90433-W

Ingall, E., & Jahnke, R. (1994). Evidence for enhanced phosphorus regeneration from marine sediments overlain by oxygen depleted waters. *Geochimica et Cosmochimica Acta*, *58*(11), 2571–2575. https://doi.org/10.1016/0016-7037(94)90033-7

Ingall, E., & Jahnke, R. (1997). Influence of water-column anoxia on the elemental fractionation of carbon and phosphorus during sediment diagenesis. *Marine Geology*, *139*(1–4), 219–229. https://doi.org/10.1016/S0025-3227(96)00112-0

Ingall, E., & Van Cappellen, P. (1990). Relation between Sedimentation-Rate and Burial of Organic Phosphorus and Organic-Carbon in Marine-Sediments. *Geochimica Et Cosmochimica Acta*, *54*(2), 373–386. https://doi.org/10.1016/0016-7037(90)90326-G

Jarvis, I., Gale, A. S., Jenkyns, H. C., & Pearce, M. A. (2006). Secular variation in Late Cretaceous carbon isotopes: a new δ13C carbonate reference curve for the Cenomanian–Campanian (99.6–70.6 Ma). *Geological Magazine*, *143*(5), 561–608. https://doi.org/10.1017/s0016756806002421

Jarvis, I., Lignum, J. S., Gröcke, D. R., Jenkyns, H. C., & Pearce, M. A. (2011). Black shale deposition, atmospheric CO_2 drawdown, and cooling during the Cenomanian-Turonian Oceanic Anoxic Event. *Paleoceanography*, *26*(3). https://doi.org/10.1029/2010pa002081

Jefferies, R. P. S. (1962). The palaeoecology of the Actinocamax plenus subzone (lowest Turonian) in the Anglo-Paris Basin. *Palaeontology*, *4*(4), 609–647.

Jenkyns, H. C. (1980). Cretaceous Anoxic events: from continents to oceans. *Journal of the Geological Society*, *137*(2), 171–188. https://doi.org/10.1144/gsjgs.137.2.0171

Jenkyns, H. C. (2010). Geochemistry of oceanic anoxic events. *Geochemistry, Geophysics, Geosystems*, *11*(3). https://doi.org/10.1029/2009gc002788

Jones, M. M., Sageman, B. B., Selby, D., Jacobson, A. D., Batenburg, S. J., Riquier, L., MacLeod, K. G., Huber, B. T., Bogus, K. A., Tejada, M. L. G., Kuroda, J., & Hobbs, R. W. (2023). Abrupt episode of mid-Cretaceous ocean acidification triggered by massive volcanism. *Nature Geoscience*, *16*(2), 169–174. https://doi.org/10.1038/s41561-022-01115-w

Jones, M. M., Sageman, B. B., Selby, D., Jicha, B. R., Singer, B. S., & Titus, A. L. (2021). Regional chronostratigraphic synthesis of the Cenomanian-Turonian Oceanic Anoxic Event 2 (OAE2) interval, Western Interior Basin (USA): New Re-Os chemostratigraphy and 40Ar/39Ar geochronology. *Geological Society of America Bulletin*, *133*(5–6), 1090–1104. https://doi.org/10.1130/B35594.1

Kolonic, S., Sinninghe Damsté, J. S., Böttcher, M. E., Kuypers, M. M. M., Kuhnt, W., Beckmann, B., Scheeder, G., & Wagner, T. (2002). Geochemical characterization of Cenomanian/Turonian black shales from the Tarfaya Basin (SW Morocco) - Relationships between palaeoenvironmental conditions and early sulphurization of sedimentary organic matter. *Journal of Petroleum Geology*, *25*(3), 325–350. https://doi.org/10.1111/j.1747-5457.2002.tb00012.x

Kolonic, S., Wagner, T., Forster, A., Sinninghe Damsté, J. S., Walsworth-Bell, B., Erba, E., Turgeon, S., Brumsack, H.-J., Chellai, E. H., Tsikos, H., Kuhnt, W., & Kuypers, M. M. M. (2005). Black shale deposition on the northwest African Shelf during the Cenomanian/Turonian oceanic anoxic event: Climate coupling and global organic carbon burial. *Paleoceanography*, *20*(1). https://doi.org/10.1029/2003pa000950

Kraal, P., Slomp, C. P., Forster, A., & Kuypers, M. M. M. (2010). Phosphorus cycling from the margin to abyssal depths in the proto-Atlantic during oceanic anoxic event 2. *Palaeogeography, Palaeoclimatology, Palaeoecology*, *295*(1–2), 42–54. https://doi.org/10.1016/j.palaeo.2010.05.014

Kuhnt, W., Chellai, E. H., Holbourn, A., Luderer, F., Thurow, J., Wagner, T., El Albani, A., Beckmann, B., Herbin, J.-P., Kawamura, H., Kolonic, S., Nederbragt, S., Street, C., & Ravilious, K. (2001). Morocco Basin's sedimentary record may provide correlations for Cretaceous paleoceanographic events worldwide. *Eos, Transactions American Geophysical Union*, *82*(33), 361–364. https://doi.org/10.1029/01eo00223

Kuhnt, W., Herbin, J. P., Thurow, J., & Wiedmann, J. (1990). Distribution of Cenomanian-Turonian Organic Facies in the Western Mediterranean and Along the Adjacent Atlantic Margin. *Deposition of Organic Facies*. https://doi.org/10.1306/st30517c10

Kuhnt, W., Holbourn, A., Gale, A., Chellai, E. H., & Kennedy, W. J. (2009). Cenomanian sequence stratigraphy and sea-level fluctuations in the Tarfaya Basin (SW Morocco). *Geological Society of America Bulletin*, *121*(11–12), 1695–1710. https://doi.org/10.1130/B26418.1

Kuhnt, W., Luderer, F., Nederbragt, S., Thurow, J., & Wagner, T. (2005). Orbital-scale record of the late Cenomanian-Turonian oceanic anoxic event (OAE-2) in the Tarfaya Basin (Morocco). *International Journal of Earth Sciences*, *94*(1), 147–159. https://doi.org/10.1007/s00531-004-0440-5

Kuhnt, W., Nederbragt, A., & Leine, L. (1997). Cyclicity of Cenomanian-Turonian organic-carbon-rich sediments in the Tarfaya Atlantic Coastal Basin (Morocco). *Cretaceous Research*, *18*(4), 587–601. https://doi.org/10.1006/cres.1997.0076

Kuroda, J., Ogawa, N. O., Tanimizu, M., Coffin, M. F., Tokuyama, H., Kitazato, H., & Ohkouchi, N. (2007). Contemporaneous massive subaerial volcanism and late cretaceous Oceanic Anoxic Event 2. *Earth and Planetary Science Letters*, *256*(1–2), 211–223. https://doi.org/10.1016/j.epsl.2007.01.027

Kuypers, M. M. M., Pancost, R. D., & Damsté, J. S. S. (1999). A large and abrupt fall in atmospheric CO_2 concentration during Cretaceous times. *Nature*, *399*(6734), 342–345. https://doi.org/10.1038/20659

Kuypers, M. M. M., Pancost, R. D., Nijenhuis, I. A., & Sinninghe Damsté, J. S. (2002). Enhanced productivity led to increased organic carbon burial in the euxinic North Atlantic basin during the late Cenomanian oceanic anoxic event. *Paleoceanography*, *17*(4). https://doi.org/10.1029/2000pa000569

Ladant, J.-B., Poulsen, C. J., Fluteau, F., Tabor, C. R., MacLeod, K. G., Martin, E. E., Haynes, S. J., & Rostami, M. A. (2020). Paleogeographic controls on the evolution of Late Cretaceous ocean circulation. *Climate of the Past*, *16*(3), 973–1006. https://doi.org/10.5194/cp-16-973-2020

Lamolda, M. A., Gorostidi, A., & Paul, C. R. C. (1994). Quantitative Estimates of Calcareous Nannofossil Changes across the Plenus Marls (Latest Cenomanian), Dover, England: implications for the generation of the Cenomanian-Turonian Boundary Event. *Cretaceous Research*, *15*(2), 143–164. https://doi.org/10.1006/cres.1994.1007

Larson, R. L. (1991). Latest pulse of Earth: Evidence for a mid-Cretaceous superplume. *Geology*, *19*(6), 547–550. https://doi.org/10.1130/0091-7613(1991)019%3C0547:Lpoeef%3E2.3.Co;2

Leckie, R. M., Bralower, T. J., & Cashman, R. (2002). Oceanic anoxic events and plankton evolution: Biotic response to tectonic forcing during the mid-Cretaceous. *Paleoceanography*, *17*(3), 13–1. https://doi.org/10.1029/2001pa000623

Leine, L. (1986). Geology of the Tarfaya oil shale deposit, Morocco. *Geologie en Mijnbouw*, *65*(1), 57–74.

Liu, J., Antler, G., Pellerin, A., Izon, G., Dohrmann, I., Findlay, A. J., Røy, H., Ono, S., Turchyn, A. V., Kasten, S., & Jørgensen, B. B. (2021). Isotopically "heavy" pyrite in marine sediments due to high sedimentation rates and non-steady-state deposition. *Geology*, *49*(7), 816–821. https://doi.org/10.1130/g48415.1

Lüning, S., Kolonic, S., Belhadj, E. M., Belhadj, Z., Cota, L., Barić, G., & Wagner, T. (2004). Integrated depositional model for the Cenomanian–Turonian organic-rich strata in North Africa. *Earth-Science Reviews*, *64*(1–2), 51–117. https://doi.org/10.1016/s0012-8252(03)00039-4

Lunt, D. J., Farnsworth, A., Loptson, C., Foster, G. L., Markwick, P., O'Brien, C. L., Pancost, R. D., Robinson, S. A., & Wrobel, N. (2016). Palaeogeographic controls on climate and proxy interpretation. *Climate of the Past*, *12*(5), 1181–1198. https://doi.org/10.5194/cp-12-1181-2016

März, C., Poulton, S. W., Beckmann, B., Küster, K., Wagner, T., & Kasten, S. (2008). Redox sensitivity of P cycling during marine black shale formation: Dynamics of sulfidic and anoxic, non-sulfidic bottom waters. *Geochimica Et Cosmochimica Acta*, *72*(15), 3703–3717. https://doi.org/10.1016/j.gca.2008.04.025

McManus, J., Berelson, W. M., Klinkhammer, G. P., Hammond, D. E., & Holm, C. (2005). Authigenic uranium: relationship to oxygen penetration depth and organic carbon rain. *Geochimica Et Cosmochimica Acta*, *69*(1), 95–108. https://doi.org/10.1016/j.gca.2004.06.023

Meyers, S. R. (2007). Production and preservation of organic matter: The significance of iron. *Paleoceanography*, *22*(4). https://doi.org/10.1029/2006pa001332

Monteiro, F. M., Pancost, R. D., Ridgwell, A., & Donnadieu, Y. (2012). Nutrients as the dominant control on the spread of anoxia and euxinia across the Cenomanian-Turonian oceanic anoxic event (OAE2): Model-data comparison. *Paleoceanography*, *27*(4). https://doi.org/10.1029/2012pa002351

Mort, H. P., Adatte, T., Föllmi, K. B., Keller, G., Steinmann, P., Matera, V., Berner, Z., & Stüben, D. (2007). Phosphorus and the roles of productivity and nutrient recycling during oceanic anoxic event 2. *Geology*, *35*(6), 483. https://doi.org/10.1130/g23475a.1

Mort, H. P., Adatte, T., Keller, G., Bartels, D., Föllmi, K. B., Steinmann, P., Berner, Z., & Chellai, E. H. (2008). Organic carbon deposition and phosphorus accumulation during Oceanic Anoxic Event 2 in Tarfaya, Morocco. *Cretaceous Research*, *29*(5–6), 1008–1023. https://doi.org/10.1016/j.cretres.2008.05.026

Mort, H. P., Slomp, C. P., Gustafsson, B. G., & Andersen, T. J. (2010). Phosphorus recycling and burial in Baltic Sea sediments with contrasting redox conditions. *Geochimica Et Cosmochimica Acta*, *74*(4), 1350–1362. https://doi.org/10.1016/j.gca.2009.11.016

Nana Yobo, L., Brandon, A. D., Holmden, C., Lau, K. V., & Eldrett, J. (2021). Changing inputs of continental and submarine weathering sources of Sr to the oceans during OAE 2. *Geochimica et Cosmochimica Acta*, *303*, 205–222. https://doi.org/10.1016/j.gca.2021.03.013

Nesbitt, H. W., & Young, G. M. (1982). Early Proterozoic Climates and Plate Motions Inferred from Major Element Chemistry of Lutites. *Nature*, *299*(5885), 715–717. https://doi.org/10.1038/299715a0

O'Brien, C. L., Robinson, S. A., Pancost, R. D., Sinninghe Damsté, J. S., Schouten, S., Lunt, D. J., Alsenz, H., Bornemann, A., Bottini, C., Brassell, S. C., Farnsworth, A., Forster, A., Huber, B. T., Inglis, G. N., Jenkyns, H. C., Linnert, C., Littler, K., Markwick, P., McAnena, A., & Wrobel, N. E. (2017). Cretaceous sea-surface temperature evolution: Constraints from TEX86 and planktonic foraminiferal oxygen isotopes. *Earth-Science Reviews*, *172*, 224–247. https://doi.org/10.1016/j.earscirev.2017.07.012

O'Connor, L. K., Jenkyns, H. C., Robinson, S. A., Remmelzwaal, S. R. C., Batenburg, S. J., Parkinson, I. J., & Gale, A. S. (2020). A Re-evaluation of the Plenus Cold Event, and the Links Between CO_2, Temperature, and Seawater Chemistry During OAE 2. *Paleoceanography and Paleoclimatology*, *35*(4). https://doi.org/10.1029/2019pa003631

Ostrander, C. M., Owens, J. D., & Nielsen, S. G. (2017). Constraining the rate of oceanic deoxygenation leading up to a Cretaceous Oceanic Anoxic Event (OAE-2: ~ 94 Ma). *Science Advances*, *3*(8), e1701020. https://doi.org/10.1126/sciadv.1701020

Owens, J. D., Gill, B. C., Jenkyns, H. C., Bates, S. M., Severmann, S., Kuypers, M. M. M., Woodfine, R. G., & Lyons, T. W. (2013). Sulfur isotopes track the global extent and dynamics of euxinia during Cretaceous Oceanic Anoxic Event 2. *Proceedings of the National Academy of Sciences*, *110*(46), 18407–18412. https://doi.org/10.1073/pnas.1305304110

Park, J., & Oglesby, R. J. (1991). Milankovitch Rhythms in the Cretaceous: A GCM modelling study. *Global and Planetary Change*, *4*(4), 329–355. https://doi.org/10.1016/0921-8181(91)90001-d

Pasquier, V., Bryant, R. N., Fike, D. A., & Halevy, I. (2021). Strong local, not global, controls on marine pyrite sulfur isotopes. *Science Advances*, *7*(9), eabb7403. https://doi.org/10.1126/sciadv.abb7403

Pasquier, V., Fike, D. A., & Halevy, I. (2021). Sedimentary pyrite sulfur isotopes track the local dynamics of the Peruvian oxygen minimum zone. *Nature Communications*, *12*(1), 4403. https://doi.org/10.1038/s41467-021-24753-x

Pasquier, V., Fike, D. A., Révillon, S., & Halevy, I. (2022). A global reassessment of the controls on iron speciation in modern sediments and sedimentary rocks: A dominant role for diagenesis. *Geochimica Et Cosmochimica Acta*, *335*, 211–230. https://doi.org/10.1016/j.gca.2022.08.037

Pasquier, V., Sansjofre, P., Rabineau, M., Revillon, S., Houghton, J., & Fike, D. A. (2017). Pyrite sulfur isotopes reveal glacial–interglacial environmental changes. *Proceedings of the National Academy of Sciences*, *114*(23), 5941–5945. https://doi.org/10.1073/pnas.1618245114

Paytan, A., Kastner, M., Campbell, D., & Thiemens, M. H. (2004). Seawater sulfur isotope fluctuations in the Cretaceous. *Science*, *304*(5677), 1663–1665. https://doi.org/10.1126/science.1095258

Pogge von Strandmann, P. A. E., Jenkyns, H. C., & Woodfine, R. G. (2013). Lithium isotope evidence for enhanced weathering during Oceanic Anoxic Event 2. *Nature Geoscience*, *6*(8), 668–672. https://doi.org/10.1038/ngeo1875

Poulsen, C. J., Barron, E. J., Arthur, M. A., & Peterson, W. H. (2001). Response of the Mid-Cretaceous global oceanic circulation to tectonic and CO_2 forcings. *Paleoceanography*, *16*(6), 576–592. https://doi.org/10.1029/2000pa000579

Poulton, S. W. (2017). Early phosphorus redigested. *Nature Geoscience*, *10*(2), 75–76. https://doi.org/10.1038/ngeo2884

Poulton, S. W. (2021). *The Iron Speciation Paleoredox Proxy*. Cambridge University Press. https://doi.org/10.1017/9781108847148

Poulton, S. W., & Canfield, D. E. (2005). Development of a sequential extraction procedure for iron: implications for iron partitioning in continentally derived particulates. *Chemical Geology*, *214*(3–4), 209–221. https://doi.org/10.1016/j.chemgeo.2004.09.003

Poulton, S. W., & Canfield, D. E. (2006). Co-diagenesis of iron and phosphorus in hydrothermal sediments from the southern East Pacific Rise: Implications for the evaluation of paleoseawater phosphate concentrations. *Geochimica Et Cosmochimica Acta*, *70*(23), 5883–5898. https://doi.org/10.1016/j.gca.2006.01.030

Poulton, S. W., & Canfield, D. E. (2011). Ferruginous Conditions: A Dominant Feature of the Ocean through Earth's History. *Elements*, *7*(2), 107–112. https://doi.org/10.2113/gselements.7.2.107

Poulton, S. W., Henkel, S., März, C., Urquhart, H., Flögel, S., Kasten, S., Sinninghe Damsté, J. S., & Wagner, T. (2015). A continental-weathering control on orbitally driven redox-nutrient cycling during Cretaceous Oceanic Anoxic Event 2. *Geology*, *43*(11), 963–966. https://doi.org/10.1130/g36837.1

Poulton, S. W., Krom, M. D., & Raiswell, R. (2004). A revised scheme for the reactivity of iron (oxyhydr)oxide minerals towards dissolved sulfide. *Geochimica Et Cosmochimica Acta*, *68*(18), 3703–3715. https://doi.org/10.1016/j.gca.2004.03.012

Poulton, S. W., & Raiswell, R. (2002). The low-temperature geochemical cycle of iron: From continental fluxes to marine sediment deposition. *American Journal of Science*, *302*(9), 774–805. https://doi.org/10.2475/ajs.302.9.774

Prauss, M. L. (2012). The Cenomanian/Turonian Boundary event (CTBE) at Tarfaya, Morocco: Palaeoecological aspects as reflected by marine palynology. *Cretaceous Research*, *34*, 233–256. https://doi.org/10.1016/j.cretres.2011.11.004

Raiswell, R., & Canfield, D. E. (1998). Sources of iron for pyrite formation in marine sediments. *American Journal of Science*, *298*(3), 219–245. https://doi.org/10.2475/ajs.298.3.219

Raiswell, R., Hardisty, D. S., Lyons, T. W., Canfield, D. E., Owens, J. D., Planavsky, N. J., Poulton, S. W., & Reinhard, C. T. (2018). The iron paleoredox proxies: A guide to the pitfalls, problems and proper practice. *American Journal of Science*, *318*(5), 491–526. https://doi.org/10.2475/05.2018.03

Raiswell, R., Newton, R., & Wignall, P. B. (2001). An indicator of water-column anoxia: Resolution of biofacies variations in the Kimmeridge Clay (Upper Jurassic, U.K.). *Journal of Sedimentary Research*, *71*(2), 286–294. https://doi.org/10.1306/070300710286

Raven, M. R., Fike, D. A., Bradley, A. S., Gomes, M. L., Owens, J. D., & Webb, S. A. (2019). Paired organic matter and pyrite δ34S records reveal mechanisms of carbon, sulfur, and iron cycle disruption during Ocean Anoxic Event 2. *Earth and Planetary Science Letters*, *512*, 27–38. https://doi.org/10.1016/j.epsl.2019.01.048

Redfield, A. C. (1958). The biological control of chemical factors in the environment. *American Scientist*, *46*(3), 230A – 221.

Reinhard, C. T., Planavsky, N. J., Gill, B. C., Ozaki, K., Robbins, L. J., Lyons, T. W., Fischer, W. W., Wang, C., Cole, D. B., & Konhauser, K. O. (2017). Evolution of the global phosphorus cycle. *Nature*, *541*(7637), 386–389. https://doi.org/10.1038/nature20772

Robinson, S. A., Dickson, A. J., Pain, A., Jenkyns, H. C., O'Brien, C. L., Farnsworth, A., & Lunt, D. J. (2019). Southern Hemisphere sea-surface temperatures during the Cenomanian-Turonian: Implications for the termination of Oceanic Anoxic Event 2. *Geology*, *47*(2), 131–134. https://doi.org/10.1130/G45842.1

Robinson, S. A., & Vance, D. (2012). Widespread and synchronous change in deep-ocean circulation in the North and South Atlantic during the Late Cretaceous. *Paleoceanography*, *27*(1). https://doi.org/10.1029/2011PA002240

Ruttenberg, K. C. (1992). Development of a sequential extraction method for different forms of phosphorus in marine sediments. *Limnology and Oceanography*, *37*(7), 1460–1482. https://doi.org/10.4319/lo.1992.37.7.1460

Ruttenberg, K. C. (2003). The global phosphorus cycle. In *Treatise on Geochemistry: Second Edition* (Vol. 8, pp. 585–643). https://doi.org/10.1016/b0-08-043751-6/08153-6

Ruttenberg, K. C. (2014). The Global Phosphorus Cycle. In *Treatise on Geochemistry* (pp. 499–558). https://doi.org/10.1016/b978-0-08-095975-7.00813-5

Ruttenberg, K. C., & Berner, R. A. (1993). Authigenic Apatite Formation and Burial in Sediments from Non-Upwelling, Continental margin Environments. *Geochimica et Cosmochimica Acta*, *57*(5), 991–1007. https://doi.org/10.1016/0016-7037(93)90035-U

Ruvalcaba Baroni, I., Topper, R. P. M., van Helmond, N. A. G. M., Brinkhuis, H., & Slomp, C. P. (2014). Biogeochemistry of the North Atlantic during oceanic anoxic event 2: role of changes in ocean circulation and phosphorus input. *Biogeosciences*, *11*(4), 977–993. https://doi.org/10.5194/bg-11-977-2014

Schenau, S. J., & De Lange, G. J. (2000). A novel chemical method to quantify fish debris in marine sediments. *Limnology and Oceanography*, *45*(4), 963–971. https://doi.org/10.4319/lo.2000.45.4.0963

Schlanger, S. O., & Jenkyns, H. (1976). Cretaceous oceanic anoxic events: causes and consequences. *Netherlands Journal of Geosciences/Geologie en Mijnbouw (Classic Papers)*.

Schmidtko, S., Stramma, L., & Visbeck, M. (2017). Decline in global oceanic oxygen content during the past five decades. *Nature*, *542*(7641), 335–339. https://doi.org/10.1038/nature21399

Scholle, P. A., & Arthur, M. A. (1980). Carbon isotope fluctuations in Cretaceous pelagic limestones: potential stratigraphic and petroleum exploration tool. *Aapg Bulletin*, *64*(1), 67–87. https://doi.org/10.1306/2F91892D-16CE-11D7-8645000102C1865D

Scholz, F., Beil, S., Flögel, S., Lehmann, M. F., Holbourn, A., Wallmann, K., & Kuhnt, W. (2019). Oxygen minimum zone-type biogeochemical cycling in the Cenomanian-Turonian Proto-North Atlantic across Oceanic Anoxic Event 2. *Earth and Planetary Science Letters*, *517*, 50–60. https://doi.org/10.1016/j.epsl.2019.04.008

Sinninghe Damsté, J. S., & Köster, J. (1998). A euxinic southern North Atlantic Ocean during the Cenomanian/Turonian oceanic anoxic event. *Earth and Planetary Science Letters*, *158*(3–4), 165–173. https://doi.org/10.1016/s0012-821x(98)00052-1

Sinninghe Damsté, J. S., van Bentum, E. C., Reichart, G.-J., Pross, J., & Schouten, S. (2010). A CO_2 decrease-driven cooling and increased latitudinal temperature gradient during the mid-Cretaceous Oceanic Anoxic Event 2. *Earth and Planetary Science Letters*, *293*(1–2), 97–103. https://doi.org/10.1016/j.epsl.2010.02.027

Slomp, C. P., Epping, E. H. G., Helder, W., & Raaphorst, W. V. (1996). A key role for iron-bound phosphorus in authigenic apatite formation in North Atlantic continental platform sediments. *Journal of Marine Research*, *54*(6), 1179–1205. https://doi.org/10.1357/0022240963213745

Slomp, C. P., Thomson, J., & de Lange, G. J. (2004). Controls on phosphorus regeneration and burial during formation of eastern Mediterranean sapropels. *Marine Geology*, *203*(1–2), 141–159. https://doi.org/10.1016/S0025-3227(03)00335-9

Slomp, C. P., & Van Cappellen, P. (2007). The global marine phosphorus cycle: sensitivity to oceanic circulation. *Biogeosciences*, *4*(2), 155–171. https://doi.org/10.5194/bg-4-155-2007

Strickland, J. D. H., & Parsons, T. R. (1972). *A practical handbook of seawater analysis* (2nd ed.). Fisheries Research Board of Canada. https://doi.org/10.25607/OBP-1791

Sturchio, N. C., Antonio, M. R., Soderholm, L., Sutton, S. R., & Brannon, J. C. (1998). Tetravalent uranium in calcite. *Science*, *281*(5379), 971–973. https://doi.org/10.1126/science.281.5379.971

Takashima, R., Selby, D., Yamanaka, T., Kuwahara, Y., Nakamura, H., Sawada, K., Ikeda, M. A., Ando, T., Hayashi, K., Nishida, M., Usami, T., Kameyama, D., Nishi, H., Kuroyanagi, A., & Gyawali, B. R. (2024). Large igneous province activity drives oceanic anoxic event 2 environmental change across eastern Asia. *Communications Earth & Environment*, *5*(1). https://doi.org/10.1038/s43247-024-01214-z

Thamdrup, B. (2000). Bacterial manganese and iron reduction in aquatic sediments. *Advances in Microbial Ecology*, 41–84. https://doi.org/10.1007/978-1-4615-4187-5_2

Thompson, J., Poulton, S. W., Guilbaud, R., Doyle, K. A., Reid, S., & Krom, M. D. (2019). Development of a modified SEDEX phosphorus speciation method for ancient rocks and modern iron-rich sediments. *Chemical Geology*, *524*, 383–393. https://doi.org/10.1016/j.chemgeo.2019.07.003

Trabucho Alexandre, J., Tuenter, E., Henstra, G. A., van der Zwan, K. J., van de Wal, R. S. W., Dijkstra, H. A., & de Boer, P. L. (2010). The mid-Cretaceous North Atlantic nutrient trap: Black shales and OAEs. *Paleoceanography and Paleoclimetology*, *25*(4). https://doi.org/10.1029/2010pa001925

Tribovillard, N., Algeo, T. J., Baudin, F., & Riboulleau, A. (2012). Analysis of marine environmental conditions based onmolybdenum–uranium covariation—Applications to Mesozoic paleoceanography. *Chemical Geology*, *324–325*, 46–58. https://doi.org/10.1016/j.chemgeo.2011.09.009

Tribovillard, N., Algeo, T. J., Lyons, T., & Riboulleau, A. (2006). Trace metals as paleoredox and paleoproductivity proxies: An update. *Chemical Geology*, *232*(1–2), 12–32. https://doi.org/10.1016/j.chemgeo.2006.02.012

Tribovillard, N., Riboulleau, A., Lyons, T., & Baudin, F. (2004). Enhanced trapping of molybdenum by sulfurized marine organic matter of marine origin in Mesozoic limestones and shales. *Chemical Geology*, *213*(4), 385–401. https://doi.org/10.1016/j.chemgeo.2004.08.011

Tsikos, H., Jenkyns, H. C., Walsworth-Bell, B., Petrizzo, M. R., Forster, A., Kolonic, S., Erba, E., Premoli Silva, I., Baas, M., Wagner, T., & Sinninghe DamstÉ, J. S. (2004). Carbon-isotope stratigraphy recorded by the Cenomanian-Turonian Oceanic Anoxic Event: correlation and implications based on three key localities. *Journal of the Geological Society*, *161*(4), 711–719. https://doi.org/10.1144/0016-764903-077

Tyrrell, T. (1999). The relative influences of nitrogen and phosphorus on oceanic primary production. *Nature*, *400*(6744), 525–531. https://doi.org/10.1038/22941

van Bentum, E. C., Hetzel, A., Brumsack, H.-J., Forster, A., Reichart, G.-J., & Sinninghe Damsté, J. S. (2009). Reconstruction of water column anoxia in the equatorial Atlantic during the Cenomanian–Turonian oceanic anoxic event using biomarker and trace metal proxies. *Palaeogeography, Palaeoclimatology, Palaeoecology*, *280*(3–4), 489–498. https://doi.org/10.1016/j.palaeo.2009.07.003

Van Cappellen, P., & Ingall, E. D. (1994). Benthic phosphorus regeneration, net primary production, and ocean anoxia: A model of the coupled marine biogeochemical cycles of carbon and phosphorus. *Paleoceanography*, *9*(5), 677–692. https://doi.org/10.1029/94pa01455

Van der Weijden, C. H. (2002). Pitfalls of normalization of marine geochemical data using a common divisor. *Marine Geology*, *184*(3–4), 167–187. https://doi.org/10.1016/s0025-3227(01)00297-3

van Helmond, N. A. G. M., Ruvalcaba Baroni, I., Sluijs, A., Sinninghe Damsté, J. S., & Slomp, C. P. (2014). Spatial extent and degree of oxygen depletion in the deep proto-North Atlantic basin during Oceanic Anoxic Event 2. *Geochemistry, Geophysics, Geosystems*, *15*(11), 4254–4266. https://doi.org/10.1002/2014gc005528

Voigt, S., Erbacher, J., Mutterlose, J., Weiss, W., Westerhold, T., Wiese, F., Wilmsen, M., & Wonik, T. (2008). The Cenomanian Turonian of the Wunstorf section (North Germany): global stratigraphic reference section and new orbital time scale for Oceanic Anoxic Event 2. *Newsletters on Stratigraphy*, *43*(1), 65–89. https://doi.org/10.1127/0078-0421/2008/0043-0065

Voigt, S., Gale, A. S., & Voigt, T. (2006). Sea-level change, carbon cycling and palaeoclimate during the Late Cenomanian of northwest Europe; an integrated palaeoenvironmental analysis. *Cretaceous Research*, *27*(6), 836–858. https://doi.org/10.1016/j.cretres.2006.04.005

Wagner, T., Hofmann, P., & Flögel, S. (2013). Marine black shale deposition and Hadley Cell dynamics: A conceptual framework for the Cretaceous Atlantic Ocean. *Marine and Petroleum Geology*, *43*, 222–238. https://doi.org/10.1016/j.marpetgeo.2013.02.005

Wedepohl, K. H. (1995). The composition of the continental crust. *Geochimica et Cosmochimica Acta*, *59*(7), 1217–1232. https://doi.org/10.1016/0016-7037(95)00038-2

Wei, G.-Y., Chen, T., Poulton, S. W., Lin, Y.-B., He, T., Shi, X., Chen, J., Li, H., Qiao, S., Liu, J., Li, D., & Ling, H.-F. (2021). A chemical weathering control on the delivery of particulate iron to the continental shelf. *Geochimica et Cosmochimica Acta*, *308*, 204–216. https://doi.org/10.1016/j.gca.2021.05.058

Westermann, S., Vance, D., Cameron, V., Archer, C., & Robinson, S. A. (2014). Heterogeneous oxygenation states in the Atlantic and Tethys oceans during Oceanic Anoxic Event 2. *Earth and Planetary Science Letters*, *404*, 178–189. https://doi.org/10.1016/j.epsl.2014.07.018

Wilson, P. A., Norris, R. D., & Cooper, M. J. (2002). Testing the Cretaceous greenhouse hypothesis using glassy foraminiferal calcite from the core of the Turonian tropics on Demerara Rise. *Geology*, *30*(7), 607–610. https://doi.org/10.1130/0091-7613(2002)030%3C0607:Ttcghu%3E2.0.Co;2

Xiong, Y., Guilbaud, R., Peacock, C. L., Cox, R. P., Canfield, D. E., Krom, M. D., & Poulton, S. W. (2019). Phosphorus cycling in Lake Cadagno, Switzerland: A low sulfate euxinic ocean analogue. *Geochimica et Cosmochimica Acta*, *251*, 116–135. https://doi.org/10.1016/j.gca.2019.02.011

Zabel, M., Schneider, R. R., Wagner, T., Adegbie, A. T., de Vries, U., & Kolonic, S. (2001). Late Quaternary climate changes in central Africa as inferred from terrigenous input to the Niger fan. *Quaternary Research*, *56*(2), 207–217. https://doi.org/10.1006/qres.2001.2261

Zhao, M.-Y., Zheng, Y.-F., & Zhao, Y.-Y. (2016). Seeking a geochemical identifier for authigenic carbonate. *Nature Communications*, *7*(1), 10885. https://doi.org/10.1038/ncomms10885

Zheng, Y., Anderson, R. F., van Geen, A., & Fleisher, M. Q. (2002). Preservation of particulate non-lithogenic uranium in marine sediments. *Geochimica Et Cosmochimica Acta*, *66*(17), 3085–3092. https://doi.org/10.1016/S0016-7037(01)00632-9

SUPPLEMENTARY MATERIALS

Supplementary Information

Download: https://ajsonline.org/article/118797-controls-on-the-termination-of-cretaceous-oceanic-anoxic-event-2-in-the-tarfaya-basin-morocco/attachment/231040.docx

Data repository

Download: https://ajsonline.org/article/118797-controls-on-the-termination-of-cretaceous-oceanic-anoxic-event-2-in-the-tarfaya-basin-morocco/attachment/231041.xlsx